

# FORCAsT-gs: Importance of stomatal conductance parameterisation to estimated ozone deposition velocity

Frederick Otu-Larbi<sup>1</sup>, Adriano Conte<sup>2</sup>, Silvano Fares<sup>3</sup>, Oliver Wild<sup>1</sup>, and Kirsti Ashworth<sup>1</sup>

<sup>1</sup>Lancaster University

<sup>2</sup>Council for Agricultural Research and Economics (CREA) - Research Centre for Forestry and Wood

<sup>3</sup>National Research Council

November 23, 2022

## Abstract

The role of stomata in regulating photosynthesis and transpiration, and hence governing global biogeochemical cycles and climate, is well-known. Less well-understood, however, is the importance of stomatal control to the exchange of other trace gases between terrestrial vegetation and the atmosphere. Yet these gases determine atmospheric composition, and hence air quality and climate, on scales ranging from local to global, and seconds to decades. Vegetation is a major sink for ground-level ozone via the process of dry deposition and the primary source of many biogenic volatile organic compounds (BVOCs). The rate of dry deposition is largely controlled by the rate of diffusion of a gas through the stomata, and this also governs the emission rate of some key BVOCs. It is critical therefore that canopy-atmosphere exchange models capture the physiological processes controlling stomatal conductance and the transfer of trace gases other than carbon dioxide and water vapour. We incorporate three of the most widely used coupled stomatal conductance-photosynthesis models into the one-dimensional multi-layer FORest Canopy-Atmosphere Transfer (FORCAsT1.0) model to assess the importance of choice of parameterisation on simulated ozone deposition rates. Modelled GPP and stomatal conductance across a broad range of ecosystems differ by up to a factor of 3 between the best and worst performing model configurations. This leads to divergences in seasonal and diel profiles of ozone deposition velocity of 1-30% and deposition rate of up to 10%, demonstrating that the choice of stomatal conductance parameterisation is critical in understanding ozone deposition.

## Hosted file

otu\_larbi\_et\_al\_forcastgs\_si.docx available at <https://authorea.com/users/541285/articles/600561-forcast-gs-importance-of-stomatal-conductance-parameterisation-to-estimated-ozone-deposition-velocity>

1 **FORCAsT-gs: Importance of stomatal conductance parameterisation to**  
2 **estimated ozone deposition velocity**

3

4 **Frederick Otu-Larbi<sup>1†</sup>, Adriano Conte<sup>2</sup>, Silvano Fares<sup>2,3</sup>, Oliver Wild<sup>1</sup>, Kirsti Ashworth<sup>1†</sup>**

5 †Joint first authors

6 <sup>1</sup>Lancaster Environment Centre, Lancaster University, Lancaster, LA1 4YQ, UK

7 <sup>2</sup>Council for Agricultural Research and Economics (CREA) - Research Centre for Forestry and  
8 Wood, Viale Santa Margherita 80, 52100 Arezzo, Italy

9 <sup>3</sup>National Research Council of Italy - Institute of BioEconomy. Via dei Taurini 19, 00185 Rome,  
10 Italy.

11 *Correspondence to:* Kirsti Ashworth (k.s.ashworth1@lancaster.ac.uk)

12

13 **Key Points:**

- 14 • Medlyn coupled stomatal conductance-photosynthesis model best reproduces observed plant  
15 productivity (GPP) across various ecosystems
- 16 • Modelled GPP and stomatal conductance across forest ecosystems differ by up to a factor of  
17 3 between different model configurations
- 18 • Ozone deposition rates could vary by ~10% depending on stomatal conductance model used  
19 with implications for estimated tropospheric ozone

20

21

22

23

24

25

26

27 **Abstract**

28

29         The role of stomata in regulating photosynthesis and transpiration, and hence governing  
30 global biogeochemical cycles and climate, is well-known. Less well-understood, however, is the  
31 importance of stomatal control to the exchange of other trace gases between terrestrial vegetation and  
32 the atmosphere. Yet these gases determine atmospheric composition, and hence air quality and  
33 climate, on scales ranging from local to global, and seconds to decades. Vegetation is a major sink  
34 for ground-level ozone via the process of dry deposition and the primary source of many biogenic  
35 volatile organic compounds (BVOCs). The rate of dry deposition is largely controlled by the rate of  
36 diffusion of a gas through the stomata, and this also governs the emission rate of some key BVOCs.  
37 It is critical therefore that canopy-atmosphere exchange models capture the physiological processes  
38 controlling stomatal conductance and the transfer of trace gases other than carbon dioxide and water  
39 vapour. We incorporate three of the most widely used coupled stomatal conductance-photosynthesis  
40 models into the one-dimensional multi-layer FORest Canopy-Atmosphere Transfer (FORCAsT1.0)  
41 model to assess the importance of choice of parameterisation on simulated ozone deposition rates.  
42 Modelled GPP and stomatal conductance across a broad range of ecosystems differ by up to a factor  
43 of 3 between the best and worst performing model configurations. This leads to divergences in  
44 seasonal and diel profiles of ozone deposition velocity of 1-30% and deposition rate of up to 10%,  
45 demonstrating that the choice of stomatal conductance parameterisation is critical in understanding  
46 ozone deposition.

47

48

49

50

51

52

53 **Plain language summary**

54

55       Plants open and close their stomata to regulate the uptake of carbon dioxide (photosynthesis)  
56 and the release of water vapour into the atmosphere. Trace gases like ozone can also enter the  
57 stomata causing damage to leaves, reducing plant growth and productivity in the process. Stomatal  
58 conductance, the measure of stomatal opening, is therefore important for assessing the concentration  
59 of ozone in the atmosphere and the impacts of pollutants on plants. It is critical that canopy-  
60 atmosphere exchange models capture the processes controlling stomatal conductance and the transfer  
61 of trace gases other than carbon dioxide and water vapour. We incorporate three widely used coupled  
62 stomatal conductance-photosynthesis models into a 1-Dimensional multi-layer model to assess how  
63 the choice of model parameters affect the rate at which ozone is deposited onto plant surfaces. We  
64 first validate the model using observation from various forests sites and then compare ozone  
65 deposition rates between the best and worst performing model at each site. We found that ozone  
66 deposition rates could vary by up 10% in response to changes in model parameters, demonstrating  
67 that the choice of stomatal conductance parameterisation is crucial in understanding ozone  
68 deposition, a major process through which ozone is removed from the troposphere.

## 69 1 Introduction

70 Photosynthesis and transpiration of the world's forests drive the carbon, hydrological and  
71 nutrient cycles, governing climate, ecosystem health and productivity, and biodiversity. Forests also  
72 serve as a sink for trace gases which are deposited onto plant surfaces and taken up through the  
73 stomata. Dry deposition of ozone is of particular importance as it represents a major sink of this  
74 tropospheric pollutant. It is also of particular concern because ozone can damage photosynthetic  
75 apparatus limiting growth and productivity. The rates of photosynthesis and uptake of ozone are both  
76 dependent on the degree of stomatal opening, referred to as stomatal conductance. Plants open and  
77 close the stomata to maintain a balance between photosynthesis (CO<sub>2</sub> uptake) and leaf transpiration  
78 (water loss), thereby regulating the exchange of CO<sub>2</sub> and water vapour between vegetation and the  
79 atmosphere (Hetherington & Woodward, 2003).

80 Gases and particles deposited on leaf surfaces may be taken up through the stomata or cuticle  
81 into the leaf tissue. Stomatal uptake is the dominant of these routes for most reactive trace gases like  
82 ozone (Royal Society, 2008). As gases diffuse through the stomata, their concentrations are reduced  
83 at the leaf surface, increasing the concentration gradient between the leaf and the atmosphere above  
84 it. This concentration gradient drives deposition and has the net effect of increasing the speed at  
85 which the gas reaches the plant surface, known as the deposition velocity. The rate of stomatal  
86 diffusion and uptake is dependent on both the diffusivity of the gas and the size of the stomata.  
87 Deposition velocities are therefore dependent on stomatal conductance: the wider the stomatal  
88 aperture the lower the resistance to diffusion through the stomata.

89 It is critical that models that couple the land surface and the atmosphere are able to accurately  
90 reproduce stomatal conductance in order to account fully for the processes driving photosynthesis  
91 and trace gas deposition rates. Many empirical and semi-empirical approaches have been developed  
92 to simulate stomatal conductance. One of the earliest and most widely used is a multiplicative model

93 (Jarvis, 1976) which reduces stomatal conductance from its potential maximum according to  
94 observed responses to changing environmental conditions. Each environmental influence is assumed  
95 independent of the others (Damour et al., 2010) and does not consider physiological interactions or  
96 feedbacks that could alter stomatal movement (Yu et al., 2004).

97         Subsequent research demonstrated that stomatal aperture was also directly regulated by  
98 current photosynthesis rate (Wong et al., 1979) leading to the development of semi-empirical  
99 coupled models that assume a linear relationship between photosynthesis ( $An$ ) and  $gs$ , and iterate to  
100 simultaneously solve for both (e.g. Ball et al., 1987). More recently, optimisation theory has been  
101 applied to these coupled photosynthesis-stomatal conductance models to replicate the ‘regulatory’  
102 role of stomata, i.e. that plants control stomatal aperture to maximize carbon gain while minimizing  
103 water loss (Medlyn et al., 2011; Cowan and Farquhar, 1977).

104         The multi-layer canopy-atmosphere model FORCAsT1.0 (FORest Canopy-Atmosphere  
105 Transfer) was initially developed as an atmospheric chemistry tool for upscaling leaf-level biogenic  
106 emissions to the canopy scale and interpreting measurement data from intensive field campaigns at  
107 forest sites (CACHE; Forkel et al., 2006). It has since been modified to better capture observed  
108 dynamics and turbulent transport (CACHE; Bryan et al., 2012) and to reflect our improved  
109 understanding of the atmospheric chemistry of biogenic volatiles, particularly in low-NOx  
110 environments (FORCAsT1.0; Ashworth et al., 2015). Parameterisations of the response of isoprene  
111 emissions to water stress and re-wetting have also been incorporated into the model and  
112 demonstrated to improve model reproduction of changes in isoprene concentrations at a temperate  
113 deciduous woodland during an extended heatwave-drought (Otu-Larbi et al., 2020a).

114         FORCAsT1.0 contains explicit representations of canopy structure and leaf distribution to  
115 directly calculate photosynthetically active radiation (PAR) extinction through the canopy layers, and  
116 hence perform a full canopy energy balance, at every timestep. The resulting vertical temperature  
117 gradient drives turbulence and mixing within the canopy, and transport of energy, momentum, and

118 mass across the canopy sub-layer into the atmospheric boundary layer above, but physiology is  
119 limited to a simple parameterisation of stomatal conductance (Ashworth et al., 2015). The model has  
120 demonstrated considerable skill in reproducing observed concentrations and fluxes of short-lived  
121 biogenic reactive trace gases and their products over short time periods at a number of Northern  
122 Hemisphere forest sites (Forkel et al., 2006; Bryan et al., 2012; 2015; Ashworth et al., 2015).  
123 However, production outweighs loss processes for some gaseous species, suggesting that either  
124 deposition rates or vertical transport out of the canopy are too slow, or foliage emissions  
125 overestimated. These processes are dependent on the rate of gas exchange through the stomata, and  
126 hence the skill of the model in capturing stomatal conductance over time periods from minutes, to  
127 hours, to seasons.

128         Explicit inclusion of physiological processes in FORCAsT1.0 has the additional benefit of  
129 enabling model performance to be evaluated against canopy-scale photosynthesis and transpiration  
130 (canopy-top fluxes of CO<sub>2</sub> and water vapour) which are routinely measured and readily available  
131 over long time periods across a wide range of ecosystems. This allows a more thorough exploration  
132 and constraint of the physical and dynamical processes occurring within the canopy than is possible  
133 from concentration and flux measurements of short-lived reactive species made during short  
134 intensive field campaigns. Constraining these processes would allow us to focus more closely on the  
135 mechanisms of the production and loss of short-lived atmospherically relevant biogenic trace gases.

136         We incorporate three parameterisations of stomatal conductance and photosynthesis into  
137 FORCAsT1.0 to assess:

138         1) the ability of different coupled stomatal conductance-photosynthesis models to reproduce  
139 observed CO<sub>2</sub> fluxes across a range of different forest ecosystems and climate regions

140         2) the divergence of simulated ozone deposition velocities and deposition rates due to  
141 differences in stomatal conductance modelling approach and parameterisation

142 We use data from five forest sites within the FLUXNET2015 dataset (Pastorello et al., 2020),  
143 the most comprehensive high-quality data available from worldwide flux networks, to evaluate the  
144 performance of each of the three stomatal conductance-photosynthesis models. The sites cover three  
145 different forest ecosystems classified by IGBP as Evergreen Broadleaf Forests (EBF), Evergreen  
146 Needleleaf Forests (ENF) and Deciduous Broadleaf Forests (DBF); and three climate regions: boreal,  
147 temperate and tropical, with two of the temperate sites further sub-classified as Mediterranean. Our  
148 ultimate goal is to understand and quantify the uncertainties in modelled gross primary productivity  
149 and ozone deposition rates due to choice of stomatal conductance model, and model parameters.  
150

151

## 152 2 Methods

### 153 2.1 FORCAsT-gs

154 The 1-D (vertical column) model, FORest Canopy-Atmosphere Transfer (FORCAsT1.0), was  
155 developed to simulate exchanges of reactive biogenic volatiles between a forest site and the  
156 atmospheric boundary layer. Previous versions (CACHE: Forkel et al., 2006; Bryan et al, 2012;  
157 2015; and FORCAsT1.0: Ashworth et al., 2015; Otu-Larbi et al., 2020a) have focused on the  
158 atmospheric processes governing the concentration and distribution of these volatiles and their  
159 oxidation products within and above the canopy. FORCAsT uses 40 vertical levels as a default, 20 of  
160 which are in the vegetation canopy space, with the remainder of the levels representing the planetary  
161 boundary layer above. The thickness of the layers increases with height, permitting greater resolution  
162 in the canopy levels, which are further sub-divided into a trunk space (10 levels) and crown space  
163 (10 levels). More details about how vegetation is treated in the model can be found in Ashworth et al.  
164 (2015).

165 Heat and mass fluxes are calculated at each model level by solving the continuity equations,  
166 shown here for (gas-phase) mass:

$$167 \quad \frac{\partial c}{\partial t} = \frac{\partial}{\partial z} \left( K \frac{\partial c}{\partial z} \right) + S_c, \quad (1)$$

168 where  $c$  is the concentration or mixing ratio of a chemical species,  $z$  is the height of the layer,  $K$  is  
169 the turbulent exchange coefficient and  $S_c$  represents all sources and sinks (i.e. emissions, deposition,  
170 chemical production and loss, and advection) of water vapour or chemical compounds. All are  
171 explicitly parameterised within the model and have been fully described by Bryan et al. (2012) and  
172 Ashworth et al. (2015). We briefly re-cap those that remain unchanged from FORCAsT1.0

173 (Ashworth et al., 2015) before fully describing the coupled stomatal conductance-photosynthesis  
174 models we have now incorporated into FORCAsT-gs.

175 Leaf-level volatile emissions are calculated for each foliated canopy layer in FORCAsT-gs  
176 following the light- and temperature-dependent emission algorithms developed by Guenther et al.  
177 (1995):

$$178 \quad F = \text{LAI} \cdot \varepsilon \cdot \gamma_{TS} \cdot \gamma_{LS}, \quad (2)$$

179 where LAI is the leaf area index in each leaf-angle class and layer,  $\varepsilon$  is the emission factor or base  
180 emission rate (i.e. at standard conditions of 30 °C and 1000  $\mu\text{mol m}^{-2} \text{s}^{-1}$  photosynthetically active  
181 radiation, PAR) and  $\gamma_{TS}$  and  $\gamma_{LS}$  are activity factors that scale the base emission rate according to  
182 actual temperature and PAR. For temperature-dependent-only emissions from specialised storage  
183 pools,  $\gamma_{TS}$  and  $\gamma_{LS}$  in Eqn. 2 is replaced by  $\gamma_{TP}$  based on Steinbrecher et al. (1999). Further details of  
184 the activity factors and parameters are presented in Ashworth et al. (2015).

185 The chemistry in FORCAsT-gs is unchanged from that described by Ashworth et al. (2015).  
186 Users can use either the Regional Atmospheric Chemistry Mechanism (RACM; Stockwell et al.,  
187 1997; Geiger et al., 2003) or the Caltech Atmospheric Chemistry Mechanism (CACM; Griffin et al.,  
188 2003, 2005; Chen et al., 2006). The former includes 84 species and 249 reactions, and the latter 300  
189 species and 630 gas-phase reactions with partitioning to aerosol via the Model to Predict the  
190 Multiphase Partitioning of Organics (MPMPO; Chen et al., 2006; Ashworth et al., 2015).

191 Vertical mixing in and above the canopy are based on Baldocchi (1988) and Gao et al. (1993)  
192 respectively, following first-order K-theory (Blackadar, 1963). Eddy diffusivity is constrained by  
193 friction velocity measurements made close to but just above the top of the canopy as K-theory breaks  
194 down in the highly turbulent canopy sub-layer (Bryan et al., 2012).

195 Deposition onto vegetated surfaces and stomatal uptake is a major sink for tropospheric  
196 ozone (Royal Society, 2008). Ozone taken up through stomata is known to diminish plant growth

197 and health leading to a decrease in productivity rates and causing billions of dollars in crop losses  
 198 annually (Ainsworth et al., 2012, Avnery et al., 2011). Stomatal conductance is a key factor  
 199 controlling ozone deposition velocity and deposition rates, and therefore the extent and severity of  
 200 damage. However, estimates of stomatal conductance are sensitive to model formulation and the  
 201 choice of model parameters used in vegetation models leading to uncertainty in estimated impacts of  
 202 O<sub>3</sub> on vegetation (Damour et al., 2010). Here, we describe how FORCAsT1.0 estimates deposition  
 203 velocity and subsequently investigate how the choice of model formulation and parameters affect  
 204 these estimates.

205 The rate of dry deposition to the soil and foliage is calculated for all gas-phase compounds  
 206 for each model layer in the canopy following the parameterisations of Wesely (1989) and Gao et al.  
 207 (1993), and is described in full in Bryan et al. (2012). Deposition is assumed to occur at a rate  
 208 dependent on a species-specific Henry's law coefficient, diffusivity relative to water vapour and a  
 209 nominal reactivity factor accounting for enhanced uptake of some species due to reactions occurring  
 210 within plant cells following uptake. Of importance here is the method of calculating the deposition  
 211 velocity within the foliar layers, based on four resistances: the quasi-laminar boundary layer at the  
 212 leaf surface ( $R_b$ ), stomatal ( $R_s$ ), mesophyll ( $R_m$ ), and cuticular ( $R_c$ ) resistances, such that for each trace  
 213 gas ( $i$ ), the deposition velocity ( $v_d$ ) at each level is:

$$214 \quad v_{d,i}(z) = \frac{1}{R_{b,i}(z) + R_s(z) \frac{D_{H_2O}}{D_i} + R_{m,i}(z)} + \frac{2}{R_{b,i}(z) + R_{c,i}(z)} \quad (3)$$

215 where  $z$  is the height of the midpoint of the model level, and  $D_{H_2O}/D_i$  (=1.6) is the ratio of the  
 216 molecular diffusivities of water to ozone (Gao et al., 1993). Resistances depend on factors such as  
 217 LAI, leaf length and the reactivity factor of the trace gas and are calculated on-line in the model.  
 218 Stomatal resistance,  $R_s$ , is deduced as the inverse of stomatal conductance (Ashworth et al., 2015).

219 Ozone deposition rate,  $D_r$ , is then calculated as:

$$220 \quad D_r = v_d \times [O_3] \quad (4)$$

221 where  $[O_3]$  is the average concentration of ozone in the canopy layers.

222 In FORCAsT1.0, stomatal conductance was calculated using the Jarvis multiplicative model.  
 223 Here we extend the Jarvis approach to include photosynthesis and incorporate two coupled stomatal  
 224 conductance-photosynthesis models into FORCAsT-gs, allowing the user to select between three  
 225 different approaches to calculating photosynthesis and stomatal conductance (see Section 2.2). In all  
 226 other respects, dry deposition remains unchanged (Bryan et al., 2012; Ashworth et al., 2015).

## 227 **2.2 Physiology: coupled stomatal conductance-photosynthesis models**

228 There are currently three distinct approaches to modelling stomatal conductance and net  
 229 photosynthesis: empirical multiplicative models that estimate stomatal conductance and thence  
 230 photosynthesis rate (e.g. Jarvis, 1976); coupled stomatal conductance-photosynthesis models that  
 231 simultaneously solve for both (e.g. Ball et al., 1987); and optimisation models that simultaneously  
 232 maximise carbon assimilation while minimising water loss (e.g. Medlyn et al., 2011). We describe  
 233 below the key aspects of the three that we incorporated into FORCAsT-gs. A more detailed  
 234 description of the mathematical formulations for each model is presented in the supplementary  
 235 information.

236 The Jarvis model (Jarvis, 1976) assumes stomatal aperture is downregulated from a  
 237 theoretical maximum by the effects of environmental conditions such as temperature, PAR, and leaf  
 238 age. The scale of each down-regulation is based on experimental observations and  $g_s$  is then  
 239 calculated as:

$$240 \quad g_s = g_{max} \times f_{phen} \times f_{light} \times \max\left\{f_{min}, \left(f_{temp} \times f_{VPD} \times f_{SWC}\right)\right\} \quad (5)$$

241 where  $g_s$  ( $\text{mol m}^{-2} \text{s}^{-1}$ ) is stomatal conductance at each model level and  $g_{max}$  ( $\text{mol m}^{-2} \text{s}^{-1}$ ) is the plant  
 242 species-specific maximum value of canopy stomatal conductance for  $\text{H}_2\text{O}$ . The scaling functions,

243  $f_{phen}$ ,  $f_{light}$ ,  $f_{temp}$ ,  $f_{VPD}$ , and  $f_{SWC}$  have values between 0 and 1 and account for the reduction in stomatal  
 244 conductance due to leaf age (phenology), photosynthetic photon flux density (PPFD,  $\mu\text{mol m}^{-2} \text{s}^{-1}$ ;  
 245 defined as the intensity of PAR reaching each square meter of the canopy per second), temperature  
 246 ( $T$ ,  $^{\circ}\text{C}$ ), vapour pressure deficit (VPD, kPa), and volumetric soil water content (SWC,  $\text{m}^3 \text{m}^{-3}$ ),  
 247 respectively.  $f_{min}$  is the minimum stomatal conductance during daylight. Details of the calculations of  
 248 each of the functions are given in S1.1.

249 Net photosynthesis rate,  $A_n$ , is then assumed to be directly proportional to the conductance,  $g_s$ ,  
 250 such that:

$$251 \quad A_n = g_s \times C_i \quad (6)$$

252 where  $C_i$  is the ratio of ambient to internal concentrations of  $\text{CO}_2$  and is normally taken as 0.7.  
 253 Parameter values for each site were determined from field measurements, lab-based experiments or  
 254 taken from literature for the nearest equivalent and are shown in Table S2.

255 The Ball-Berry coupled stomatal conductance-photosynthesis model assumes that stomatal  
 256 conductance is regulated directly by the instantaneous rate of photosynthesis to balance  $\text{CO}_2$   
 257 concentrations inside the leaf with ambient levels. Photosynthesis rate ( $A$ ;  $\mu\text{mol m}^{-2} \text{s}^{-1}$ ) at each level  
 258 in the canopy is calculated following the formulations of Farquhar et al. (1980), Harley et al. (1992)  
 259 and Baldocchi (1994):

$$260 \quad A = V_c - 0.5 V_o - R_d \quad (7)$$

261 where  $V_c$  is the carboxylation rate,  $V_o$  the oxygenation rate,  $R_d$  the dark respiration rate and

$$262 \quad V_c - 0.5 V_o = \min[A_c, A_j] \times (1 - \Gamma / C_i) \quad (8)$$

263 i.e. assuming that photosynthesis rate is limited by either Ribulose biphosphate saturation during  
 264 carboxylation ( $A_c$ ) or by the rate of electron transport for Ribulose biphosphate regeneration during  
 265 oxygenation ( $A_j$ ).  $\Gamma$  is the  $\text{CO}_2$  compensation point (the  $\text{CO}_2$  concentration at which net  $\text{CO}_2$  fixation

266 is zero at a given O<sub>2</sub> level and temperature (Moss et al., 1969)) in the absence of dark respiration, and  
267 C<sub>i</sub> is the intercellular CO<sub>2</sub> concentration (Farquhar and von Caemmerer, 1982).

268 The internal CO<sub>2</sub> concentration of the leaf, C<sub>i</sub> is:

$$269 \quad C_i = C_s - \frac{A}{g_s} \quad (9)$$

270 where g<sub>s</sub> is stomatal conductance and C<sub>s</sub> is the CO<sub>2</sub> concentration at the leaf surface. Here, g<sub>s</sub> was  
271 calculated following Ball et al. (1987) as:

$$272 \quad g_s = g_o + m \frac{A * RH}{C_s} \quad (10)$$

273 where g<sub>o</sub> is the residual stomatal conductance as A tends to zero, m is a species-specific coefficient  
274 expressing the sensitivity of g<sub>s</sub> to changes in A, and RH is the relative humidity at the leaf surface.

275 Medlyn et al. (2011) also assume that photosynthesis rate at each level in the canopy is the  
276 minimum of carboxylation and electron transport rate. The version incorporated into FORCAsT-gs is  
277 based on the parameterisations of Farquhar et al. (1980) for photosynthesis rate (A; μmol m<sup>-2</sup> s<sup>-1</sup>) in  
278 C3 plants such that:

$$279 \quad A = \min(A_j, A_c) - R_d \quad (11)$$

280 where R<sub>d</sub> (mol m<sup>-2</sup> s<sup>-1</sup>) is the leaf dark respiration.

281 Stomatal conductance (g<sub>s</sub>) is then modelled following optimisation theory (Medlyn et al.,  
282 2011) in which stomatal aperture is regulated to maximise carbon gain while simultaneously  
283 minimising water loss:

$$284 \quad g_s \approx g_o + \left(1 + \frac{g_i}{\sqrt{D}}\right) \frac{A}{C_s} \quad (12)$$

285 where  $g_o$  ( $\text{mol m}^{-2} \text{s}^{-1}$ ) is the residual stomatal conductance as  $A$  approaches zero and  $g_l$  is the slope  
286 of the sensitivity of  $g_s$  to changes in  $A$ .  $D$  (kPa) is the vapour pressure deficit and  $C_s$  ( $\mu\text{mol mol}^{-1}$ ) the  
287  $\text{CO}_2$  concentration at the leaf surface as before. The values of  $g_o$  and  $g_l$  are determined at the species-  
288 or PFT-level from experimental data, and in this study were obtained from Lin et al. (2015) and De  
289 Kauwe et al. (2015). Values for each site are listed in Tables S2.

290 The Jarvis model includes soil moisture stress as one of the factors limiting stomatal  
291 conductance. The relationship between SWC and  $g_s$  is modelled following B ker et al. (2015):

$$f_{\text{SWC}} = \frac{\theta - \theta_w}{\theta_f - \theta_w} \quad (13)$$

293  
294 where PAW is plant available water and is given by:

$$PAW = \frac{\theta - \theta_w}{\theta_f - \theta_w} \quad (14)$$

296 where  $\theta$  is the volumetric soil water content (SWC,  $\text{m}^3 \text{m}^{-3}$ ),  $\theta_f$  and  $\theta_w$  are the SWC at field capacity  
297 and wilting point respectively, and  $PAW_t$  is a site-specific threshold of the fraction of water in the  
298 soil that is available to the plant estimated from site soil characteristics.

299 For both the Ball-Berry and Medlyn models, we assumed the effect of water stress on  
300 photosynthesis to be the result of biochemical limitations as demonstrated in previous studies (e.g  
301 see Egea et al., 2011). A soil moisture stress function ( $\beta$ ) was therefore applied to the maximum rate  
302 of RuBP carboxylation ( $V_{\text{cmax}}$ ) and the maximum rate of electron transport ( $J_{\text{max}}$ ) to reflect the impact  
303 of soil moisture deficit on plant gas exchange.

304  $\beta$  ranges between 1 (in the absence of water stress) to 0 (at wilting point) and is calculated based on  
 305 soil water content following Porporato et al. (2001); Keenan et al. (2009); Keenan et al. (2010):

$$306 \quad \beta = \begin{cases} 1 & \text{for } \theta \geq \theta_C \\ \left[ \frac{\theta - \theta_w}{\theta_C - \theta_w} \right]^q & \text{for } \theta_w < \theta < \theta_C \\ 0 & \text{for } \theta < \theta_w \end{cases} \quad (15)$$

307 where  $\theta$  ( $\text{m}^3 \text{m}^{-3}$ ) is the volumetric soil moisture,  $\theta_w$  is the wilting point ( $\text{m}^3 \text{m}^{-3}$ ), and  $\theta_c$  is a critical  
 308 soil moisture content above which water stress is found not to affect plant-atmosphere  $\text{CO}_2$  and water  
 309 vapour exchange (Egea et al., 2011).  $q$  is a site-specific empirical factor describing the non-linearity  
 310 of the effects of soil water stress on tree physiological processes, and here, was derived from  
 311 observations at each site.

312 Photosynthesis and stomatal conductance are then estimated using the water-stressed values  $V_{cmax^*}$   
 313 and  $J_{max^*}$ :

$$314 \quad V_{cmax^*} = V_{cmax} \times \beta \quad (16a)$$

$$315 \quad J_{max^*} = J_{max} \times \beta \quad (16b)$$

316 The Medlyn model further assumes direct limitation to stomatal conductance due to water  
 317 stress following De Kauwe et al. (2015), such that, stomatal conductance becomes:

$$318 \quad g_s \approx g_o + \left( 1 + \frac{g_{1\beta}}{\sqrt{D}} \right) \frac{A}{C_s} \quad (17)$$

319 These soil moisture stress functions are applied in all of the simulations conducted here.

### 320 2.3 FLUXNET sites

321 An overview of the five sites is given below with further information provided in Table S1  
 322 and Figure S1. The sites are included in the FLUXNET2015 dataset which categorises each location

323 by IGBP ecosystem type (Loveland et al., 2000). “Forests” indicates >60% of landcover is woody  
324 vegetation at least 2 m in height. “Evergreen Forests” retain green foliage throughout the year, while  
325 “Deciduous Forests” exhibit a seasonal cycle in which there are periods with foliage on the trees and  
326 other periods when there is no foliage.

### 327 **2.3.1 Santarém-Km67-Primary Forest (BR\_Sa1)**

328 BR\_Sa1 is in Amazonian Brazil and consists of primary forest comprising a wide range of  
329 tree species of varied ages, epiphytes, and high numbers of decaying logs. A flux tower, which was  
330 established in 2000 for the Large-scale Biosphere-Atmosphere (LBA) experiment (Rice et al., 2004)  
331 is sited on a large level plateau with forest cover stretching 5-40 km in all directions (Goulden et al.,  
332 2004). There is closed-canopy forest to an average height of 40 m within the footprint of the flux  
333 tower, with numerous emergent trees up to 55m in height (Rice et al., 2004).

334 Figure 1 shows volumetric soil moisture and meteorological data from BR\_Sa1 (yellow line)  
335 for an average annual profile. The site is categorised as Tropical Evergreen Forest and has a hot  
336 humid tropical environment with average rainfall of 1920 mm y<sup>-1</sup> and relative humidity of 85%  
337 (Parotta et al., 1995). Although a number of intense precipitation events occur during the dry season  
338 (Aug-Dec each year), the majority of the rainfall occurs during the wet season (Dec-Jul) with  
339 maximum intensity between 13h00-16h00 local time (da Rocha et al., 2004). Annual average  
340 temperature is ~25°C, with little diurnal or seasonal variability (Rice et al., 2004). Daily maximum  
341 temperatures range between 24-32°C and minimum 20-25°C. The wet season is ~1-3°C cooler than  
342 the dry, with incoming solar radiation substantially lower due to cloud cover (da Rocha et al., 2004).

343 The clay soil has little organic content and retains water well. Soil moisture is not routinely  
344 measured at BR\_Sa1 and we use data from a nearby site (BR\_Sa3 at the 83 km marker) located in  
345 the same area of forest. A selective logging experiment commenced at BR\_Sa3 shortly after the main  
346 LBA campaign and has continued to this day. Less than 5% of aboveground biomass is removed

347 each time, leaving only small gaps between areas of closed-canopy forest (Goulden et al., 2004). Soil  
348 moisture at 5 cm depth at BR\_Sa3 responds quickly to precipitation, ranging between  $\sim 0.30\text{-}0.47\text{ m}^3$   
349  $\text{m}^{-3}$ . At a depth of 250 cm, there is little variation with soil moisture relatively constant at  $\sim 0.46\text{ m}^3$   
350  $\text{m}^{-3}$  during the wet season, declining gradually to  $\sim 0.42\text{ m}^3\text{ m}^{-3}$  by the end of the dry season (Rice et  
351 al., 2004).

### 352 2.3.2 Hyytiälä (FI\_Hyy)

353 FI\_Hyy is located in the sub-boreal climate zone at the SMEAR II (Station for Measuring  
354 Ecosystem-Atmosphere Relation) boreal forest research station at Hyytiälä,  $\sim 220\text{ km}$  NW of Helsinki  
355 (Hari and Kulmala, 2005; Rinne et al., 2007). The 73-m flux tower is situated on relatively level  
356 ground, surrounded by predominantly uniform age ( $\sim 60\text{-year-old}$ ) Scots pine (*Pinus sylvestris*) with  
357 an average canopy height of 14 m (Hari and Kulmala, 2005; Suni et al., 2003).

358 Figure 1 shows volumetric soil moisture and meteorological data from FI\_Hyy (blue line) for  
359 an average year. The site is categorised as Boreal Evergreen Forest with climatological (1959-2014)  
360 average annual temperature of  $3.5^\circ\text{C}$  and precipitation of  $693\text{ mm y}^{-1}$  falling predominantly as snow  
361 during the winter months (Suni et al, 2003; SMEARII, 2021). Average monthly temperatures range  
362 between  $-7.7^\circ\text{C}$  in February, and  $16^\circ\text{C}$  in July (SMEARII, 2021). Prevailing winds are SSW and are  
363 generally moderate, with average annual windspeed of  $\sim 2.8\text{ m s}^{-1}$  and maximum of  $14\text{ m s}^{-1}$   
364 (SMEARII, 2021). The soil comprises sandy and coarse silty glacial till (Suni et al., 2003). Soil  
365 moisture peaks at  $>0.45\text{ m}^3\text{ m}^{-3}$  after snow melt and drops to  $\sim 0.30\text{ m}^3\text{ m}^{-3}$  or lower during occasional  
366 summer droughts.

### 367 2.3.3 Castelporziano (IT\_Cp2)

368 IT\_Cp2 is located at “Grotta di Piastra” within the Presidential Estate at Castelporziano, on  
369 the Tyrrhenian coast  $\sim 25\text{ km}$  SW of Rome. The 6000 ha Estate has been used for environmental  
370 research since 1951 with a flux tower first installed in 1996. The current tower is  $\sim 20\text{ m}$  tall and

371 surrounded almost exclusively by even-aged Holm oak (*Quercus ilex*) of average ~14 m height  
372 (Fares et al., 2019). This is a typical macchia species, well-adapted to an environment characterised  
373 by hot dry summers and nutrient-poor sandy soils (Fares et al., 2009).

374 Figure 1 shows volumetric soil moisture and meteorological data from IT\_Cp2 (red line) for  
375 an average year. The site is categorised as Temperate Evergreen Forest and has a Mediterranean  
376 environment with an average rainfall of 745 mm y<sup>-1</sup> of which <100 mm y<sup>-1</sup> falls in the summer  
377 months (May-early September). Between 1996-2011, mean monthly temperatures ranged between  
378 8.4-24.7°C, with a maximum temperature of 30.3 °C and minimum of 5.0 °C recorded in August and  
379 February respectively (Fusaro et al., 2015).

380 The soil is sandy and freely draining. Soil moisture is thus highly variable and tightly coupled  
381 to precipitation events. Soil moisture averaged over a depth of 10-50 cm ranges from ~5% at the end  
382 of the summer drought period to ~32% during the winter (Fares et al., 2019).

#### 383 **2.3.4 Blodgett Forest (US\_Blo)**

384 US\_Blo is located in a uniform-age Ponderosa pine plantation in the Sierra Nevada mountain  
385 range on the western coast of the continental USA. The plantation was established in 1990 and a 15-  
386 m flux tower, which has been the site of long-term monitoring and numerous intensive field  
387 campaigns, erected in 1997 (Goldstein, 2000). The average height of the canopy is ~9 m (Park et al.,  
388 2014).

389 Figure 1 shows volumetric soil moisture and meteorological data from US\_Blo (black line)  
390 for an average year. The site is categorised as Temperate Evergreen Forest with a Mediterranean  
391 climate. Annual average precipitation is ~1630 mm y<sup>-1</sup> with little rain during the summer months  
392 (May-early September). Average daily temperatures range between 17-24 °C in the summer, and 0-9  
393 °C in the winter (Goldstein, 2000).

394 The soil is predominantly free draining loam, and soil moisture tracks precipitation  
395 (Goldstein, 2000). Average soil moisture at a depth of 10-20 cm ranges from  $\sim 0.10 \text{ m}^3 \text{ m}^{-3}$  during  
396 summer droughts to just below  $0.35 \text{ m}^3 \text{ m}^{-3}$  in the winter.

### 397 2.3.5 Harvard Forest (US\_Ha1)

398 US\_Ha1 is located within a  $\sim 1600$  ha area of old-growth (75+ years) mixed forest in NE  
399 USA that has been the site of long-term ecological and environmental monitoring since 1907. A 30-  
400 m flux tower was erected in 1990 and has been used for continuous measurements and summer field  
401 campaigns since (Goldstein et al., 1998; McKinney et al., 2011). The average height of the canopy is  
402  $\sim 24$  m (Clifton et al., 2019)

403 Figure 1 shows volumetric soil moisture and meteorological data from US\_Ha1 (grey line)  
404 for an average year. The site is categorised as Temperate Deciduous Forest with the footprint of the  
405 tower dominated by red oak (*Quercus rubra*) and red maple (*Acer rubrum*), although there are a  
406 number of red and white pines (*Pinus resinosa* and *P. strobus*) to the NW of the tower (Clifton et al.,  
407 2019).

408 The site has been shown to be relatively homogeneous in all directions from the tower with  
409 energy budget closure achieved to within 20% (Goldstein et al., 1998). Annual average precipitation  
410 is  $\sim 1000 \text{ mm y}^{-1}$  and is relatively evenly distributed through the year. Average daily temperatures  
411 range between  $\sim 20$  °C in the summer, and  $\sim 1$  °C in the winter.

412 The soil around the flux tower is a sandy loam (Allen, 1995). Soil moisture typically ranges  
413 from  $\sim 0.25\text{-}0.55 \text{ m}^3 \text{ g}^{-3}$ , but can drop below  $0.20 \text{ m}^3 \text{ m}^{-3}$  during (infrequent) drought years (Clifton et  
414 al., 2019).

## 415 2.4 Simulations

416 Stomatal conductance, photosynthesis rate (instantaneous fluxes of  $\text{CO}_2$ ) and deposition  
417 velocity are calculated for each leaf angle class (9 sunlit and 1 shaded) for each foliage-containing

418 level within the canopy in FORCAsT-gs using each of the three physiological approaches outlined in  
419 Section 2.2. These are then weighted by leaf angle fraction and leaf area distribution at each level  
420 and summed over all model layers to obtain canopy-scale conductance, photosynthesis rates  
421 (canopy-top fluxes of CO<sub>2</sub>) and deposition velocity. FLUXNET2015 sites report the total rate of  
422 photosynthesis throughout the canopy as Gross Primary Productivity (GPP), deduced from the  
423 Penrose-Monteith physiology model. We therefore evaluate model performance via comparison of  
424 modelled canopy CO<sub>2</sub> fluxes to measured GPP.

425         During preliminary model configuration at each site, site-specific phenological and canopy  
426 structure were set to best fit modelled to observed GPP. However, the physiological parameters used  
427 in each of the three coupled stomatal conductance-photosynthesis algorithms were set to average  
428 values reported from previous studies in-situ at similar ecosystems or in controlled environments.  
429 These semi-optimised configurations provided our baseline simulations at each site (hereafter  
430 referred to as BASE).

431         To determine the sensitivity of the model to perturbations in the physiological parameters,  
432 which are mostly derived from controlled environment experiments, and to provide uncertainty  
433 bounds for our estimates of GPP and ozone deposition rates, we conducted a series of sensitivity  
434 tests. Only parameters with a direct relationship to stomatal conductance were used in these  
435 sensitivity tests to ensure consistency in approach.

436         In the Jarvis multiplicative model, stomatal conductance is estimated by scaling the  
437 maximum conductance observed in saturating light conditions ( $g_{max}$ ; Eqn. 5) according to  
438 environmental and phenological limitations. Average values of  $g_{max}$  for specific plant functional types  
439 are generally used, but Hoshika et al. (2018) found variations of up to 70 % between the upper and  
440 lower bounds of  $g_{max}$  and the mean for different PFTs. Here, we use the mean values for different

441 forest ecosystems for baseline simulations (JV) and the upper and lower bounds as JV+ and JV-  
442 respectively (Table S1).

443 For the Ball-Berry coupled stomatal conductance-photosynthesis model, the coefficient  $m$   
444 (Eqn. 10) describing the relationship between stomatal conductance and photosynthesis typically  
445 ranges between 9 and 12. We use these as our lower (BB-) and upper (BB+) bounds, with the  
446 baseline (BB) set to a value of 10. See Table S3 for further details of parameter settings.

447 The equivalent coefficient,  $g_l$  (Eqn. 12), is tested in the Medlyn optimisation model. We take  
448 the upper (MD+) and lower (MD-) bounds of  $g_l$  as reported by De Kauwe et al. (2015) and Lin et al  
449 (2015) for different forest ecosystems with error margins of 2-10%. Our baseline simulations (MD)  
450 use the average value for each site. Further details of parameter settings are given in Table S3.

451 Simulations for each site were driven with observed half-hourly meteorological and  
452 environmental conditions for as many years as the site has been active (see Table 1). At the end of  
453 the simulation period, average annual and diel profiles of total canopy photosynthesis were  
454 calculated and compared with observed GPP. To assess the relative performance of each model at  
455 each of the five sites, we define a single summary statistic, that reduces the three individual Taylor  
456 model performance indicators to a single value. This summary statistic is the product of the  
457 difference between modelled and observed Taylor statistics calculated as:

$$458 \quad \text{Summary} = cRMSE \times (1.0 - r^2) \times |normSD - 1.0| \quad (18)$$

459 where  $r^2$  is Pearson's correlation coefficient, normSD the normalised standard deviation and cRMSE  
460 the centred root mean square error. The closer this value is to zero, the closer the model fit to  
461 observations.

462

## 463 3 Results

### 464 3.1 BASE

465 We first evaluate the skill of each of the three stomatal conductance-photosynthesis models to  
466 reproduce the average diel and annual profiles of GPP at each site for the time periods shown in  
467 Table S1. The BASE simulations presented here use the parameter values given in Table S2.

468

#### 469 3.1.1 Jarvis (JV)

470 As shown by the orange lines on Figure 2, the multiplicative stomatal conductance model  
471 (JV) reproduces the seasonal variation in GPP at all sites except for BR\_Sa1, although it  
472 substantially overestimates seasonal GPP at the three broadleaf forests (BR\_Sa1, IT\_Cp2 and  
473 US\_Ha1) and underestimates at the Boreal needleleaf forest (FI\_Hyy). At BR\_Sa1, JV overestimates  
474 GPP by a factor of 1.5-2. At IT\_Cp2 and US\_Ha1, however, while JV overestimates GPP by 50-  
475 100% in spring and summer it performs well in the rest of the year. For FI\_Hyy, JV consistently  
476 underestimates productivity from summer through to early autumn, by a factor of 2. However, the  
477 model reproduces GPP at US\_Blo, which is also a needleleaf forest, to within 20% of the  
478 observations at all times of the year. This suggests that the phenology of Boreal ecosystems is not  
479 well-captured.

480 The diel profiles of modelled GPP using JV follows a similar inter-site pattern to that of the  
481 seasonal profile with overestimation of diurnal GPP at BR\_SA1, IT\_Cp2 and US\_Ha1 by 5-200%,  
482 and underestimation of ~75% at FI\_Hyy.

483 Of the three, JV is the poorest performer across all the sites. The summary statistics shown in  
484 Table S4 ranges from 0.02 at US\_Blo where JV performed well at reproducing observed GPP to  
485 28.86 at BR\_Sa1 where it overestimates both seasonal and diurnal profile of GPP. Seasonal cRMSE

486 ranging between 1.24-10.64, normSD between 0.40-3.72 and  $r^2$  as low as 0.01 at BR\_Sa1, further  
487 confirms the relatively poor performance of this model.

488

### 489 **3.1.2 Ball Berry (BB)**

490 The coupled stomatal conductance-photosynthesis model (BB) reproduces the observed  
491 seasonality and magnitude of GPP within 10-50% at all but the tropical BR\_Sa1 ecosystem as shown  
492 by the brown lines on the first column of Figure 2. BB underestimates summer GPP at FI\_Hyy by  
493 30% but overestimates GPP at IT\_Cp2 by a similar margin in the summer when seasonal drought  
494 occurs. It closely matches observed GPP throughout the season at US\_Blo and US\_Ha1 with <10%  
495 variation between model estimates and observations. Although BB overestimates GPP by as much as  
496 50% at BR\_Sa1 throughout the year, it outperforms both JV and MD at this site.

497 The diurnal profile of GPP estimated by BB confirms its superior performance at the tropical  
498 site BR\_Sa1, with modelled GPP closely matching the observations during the day. The diurnal  
499 profile at the other sites shows that BB underestimates GPP by ~5% in the early hours of the day at  
500 FI\_Hyy and IT\_Cp2 but tends to overestimate GPP by ~20% in the later afternoons.

501 As shown by the Summary statistic in Table S4, which ranges between 0.01 and 0.99, BB  
502 outperforms JV at all sites. As summarised by the Taylor diagram in Figure 3, BB's performance is  
503 better than that of JV, with cRMSE of 1.07 - 2.47,  $r^2$  of 0.85-0.97 (excluding BR\_Sa1) and normSD  
504 of 0.80-1.82.

505

### 506 **3.1.3 Medlyn (MD)**

507 Output from the Medlyn model (MD) is shown in blue in Figure 2. While MD follows the  
508 seasonal fluctuation of GPP at BR\_Sa1, estimated fluxes are a factor of ~1.5 higher than  
509 observations throughout the year. This overestimation of GPP at the tropical site is also apparent in  
510 the profile over the course of an average day. By contrast, at the two Mediterranean sites, MD

511 reproduces both the observed seasonal and diurnal profile of GPP and is within 20% of the observed  
512 values at any time during the year or day. MD also shows excellent agreement with both the  
513 magnitude and timing of observed GPP throughout the year at FI\_Hyy but overestimates the average  
514 diurnal profile of GPP by ~20%. MD performs best at the temperate deciduous forest site, US\_Ha1,  
515 where there is <5% between model estimates and observations across both the year and day.

516 The superior performance of MD across sites is confirmed by the Taylor diagrams in Figure 3  
517 and the summary statistics in Table S4. MD exhibits high correlation (0.56-0.98), and low deviations  
518 (1.01-1.92) and error (0.90-3.03). Summary statistics ranging between 0.0003 and 1.25 confirm it as  
519 the best performing model overall.

520 These results show that MD provides the best estimates of GPP at four of the five forest sites  
521 used in this study (FI\_Hyy, IT\_Cp2, US\_Blo and US\_Ha1) while BB was the overall best performer  
522 at BR\_Sa1. JV was the least skilful of the three models, substantially overestimating GPP at  
523 BR\_Sa1, IT\_Cp2, US\_Ha1 and underestimating at FI\_Hyy. All three BASE models were most  
524 successful in reproducing observed GPP at the temperate deciduous forest, US\_Ha1, and poorest at  
525 the tropical forest, BR\_Sa1.

526

527

### 528 **3.2 Sensitivity of stomatal conductance to model parameters**

529 The BASE simulations used mid-range values for species-specific parameters  $g_{max}$  (JV; Eqn.  
530 5),  $m$  (BB; Eqn. 10), and  $g_l$  (MD; Eqn. 12). As described in Section 2.4, we carried out sensitivity  
531 tests using lower and upper bound estimates for these parameters. Here we analyse the effect that  
532 those parameter changes have on estimated photosynthesis rates for each of the three models,  
533 identifying similarities and differences in responses between sites and providing an estimate of  
534 uncertainty bounds for GPP and stomatal conductance in each case.

535

536

### 537 3.2.1 JV

538 The plant species-specific theoretical maximum value of canopy stomatal conductance for  
539 H<sub>2</sub>O ( $g_{max}$ ; Eqn 5) is central to the performance of the JV model in reproducing observed plant gas  
540 exchange. Changes in  $g_{max}$  lead to proportional changes in both stomatal conductance (Figure S4) and  
541 GPP (Figure 4) at all sites. In general, decreasing  $g_{max}$  to its lower limit decreases GPP by between  
542 ~75-120% depending on the site, while an increase to the upper bound increases GPP by similar  
543 magnitudes.

544 At the tropical and temperate forests (BR\_Sa1, IT\_Cp2, US\_Blo and US\_Ha1) where JV  
545 over-estimated GPP, using instead the lower limit of  $g_{max}$  (JV-) provided the best model-observation  
546 fit in both seasonal and diel cycles at BR\_Sa1, but substantially underestimated GPP at IT\_Cp2,  
547 US\_Blo and US\_Ha1.

548 By contrast, at FI\_Hyy, where JV underestimated GPP, the use of the upper bound of  $g_{max}$   
549 (JV+) reduced, but did not completely overcome, model underestimation through the seasons or over  
550 the course of an average day. JV+ modelled GPP was around half to two-thirds of observed fluxes, a  
551 substantial improvement on the factor of 2 underestimations in JV.

552 As shown by the Taylor plots presented in Figure 3, and Table S4, both normalised SD and  
553 centred RMSE are substantially increased in JV-. While this is a major improvement in overall  
554 model performance at BR\_Sa1 (with cRMSE reduced from 10.6 in JV to 2.36 in JV-), JV-  
555 substantially worsens model fit at all the other sites. JV+ exacerbates the tendency to over-estimation  
556 across all sites, with Summary statistics increasing to 0.22-87.40. The correlation coefficient between  
557 modelled and measured GPP is unchanged as it essentially summarises the temporal fit.

558

559

### 560 3.2.2 BB

561 For both the BB and MD parameterisations, stomatal conductance and net photosynthesis rate  
562 are explicitly linked and solved simultaneously. Variations in species-specific response parameters  
563 therefore directly affect both  $g_s$  and GPP. Similarly to JV, the upper bound increased and lower  
564 bound reduced flux estimates compared to the baseline.

565 In BB, increasing  $m$ , i.e. the change in photosynthesis rate for a given change in stomatal  
566 conductance, results in proportionally larger increases in GPP than the decreases resulting from  
567 reducing  $m$ . GPP was slightly over-estimated by BB at all sites (except during the summer months at  
568 FI\_Hyy where modelled fluxes were lower than observed). BB- therefore provides a better fit to  
569 observed GPP across all sites except FI\_Hyy where BB+ performed better. It should be noted  
570 however, that changes in GPP (0.5-1.0%) are considerably smaller than those observed for JV  
571 between the upper and lower bound simulations.

572 This is further corroborated by the Taylor diagrams (Figure 3) summarising the average,  
573 upper and lower bound simulations. Across all sites, there was little change in correlation between  
574 estimated and observed GPP, reflecting the minor changes in temporal profile. NormSD also  
575 remained virtually unchanged between simulations for GPP fluxes (~1.0 at US\_Blo and US\_Ha1,  
576 ~0.8 at FI\_Hyy and ~2.0 at IT\_Cp2). cRMSE is consistently low for all simulations at the extra-  
577 tropical sites (~1.0-1.2 for GPP at US\_Blo and FI\_Hyy, and 1.4-1.8 at IT\_Cp2 and US\_Ha1),  
578 indicating the relatively good match to absolute values. By contrast, cRMSE remained high (>2.5) at  
579 the tropical rainforest site, BR\_Sa1, where a high normSD and low correlation coefficient also  
580 confirm the poor performance of the model at capturing both the magnitude and temporal variations  
581 in GPP at this ecosystem. The BASE simulation BB proved the closest fit to observed GPP at  
582 BR\_Sa1.

583

### 584 3.2.3 MD

585 Similarly to BB, changes in  $g_l$  in MD result in very small changes in estimated GPP. At the  
586 two Mediterranean sites (IT\_Cp2 and US\_Blo) where GPP was over-estimated by the baseline (MD)  
587 simulations, MD- provides a closer fit to observations (Figure 3) although the change is only ~1%.  
588 Changes in  $g_l$  have a negligible effect on GPP at BR\_Sa1, FI\_Hyy or US\_Ha1 (Figure 3), where  
589 droughts are rare and there is less need for plants to conserve water, i.e. where there is less conflict  
590 between maximising photosynthesis and minimising transpiration.

591 As shown by the Taylor diagrams (Figure 3), increasing the value of  $g_l$  from the average  
592 (10.0) to the upper bound (12.0) improves the correlation between estimated and observed GPP at  
593 US\_Blo, while decreasing the value improves the fit slightly at IT\_Cp2. As suggested by the  
594 temporal profiles, there is no noticeable change in correlation at BR\_Sa1, FI\_Hyy or US\_Ha1. The  
595 normSD for GPP are very close to 1.0 (i.e. a perfect fit to observations) and centred RMSE <0.5 at  
596 FI\_Hyy, US\_Ha1 and US\_Blo but near 2.0 and 1.0 respectively at IT\_Cp2, again likely a result of  
597 the severity of droughts at Castelporziano, where water conservation is a key driver of stomatal  
598 conductance. All three statistics remain poor at BR\_Sa1, where  $r^2$  remains virtually unchanged at  
599 ~0.6, normSD at 2.0, and cRMSE at ~1.8 for all values of  $g_l$ . Considering the relatively small  
600 changes observed in GPP in response to changes in  $g_l$ , we conclude that the mean values of  $g_l$  are  
601 sufficient for estimating stomatal conductance and GPP using the Medlyn model at these sites.

602

### 603 3.2.4 Summary of sensitivity tests

604 As shown by Figures 3 and 4, and Table S4, GPP estimates in JV were more sensitive to  
605 variations in  $g_{max}$  than BB and MD estimates were to  $m$  and  $g_l$ , respectively. However, modelled GPP  
606 does not vary by the same magnitude as the variation in model parameters. For instance, modelled  
607 GPP values in JV- and JV differed from BASE (JV) estimates by as much as 100% in response to up  
608 to 60% variation in  $g_{max}$  causing substantially differences in model output statistics (Figure 3 and

609 Table S4). GPP estimates using upper and lower bounds of  $m$  (BB) and  $g_l$  (MD) only differed by 1-  
610 5% in response to a 10-20% change in the model parameterisation. It must be noted that these  
611 sensitivity tests only focused on stomatal conductance parameters in all three models. Tests  
612 conducted on photosynthetic parameters such as  $V_{cmax}$  and  $J_{max}$  have shown a greater difference in  
613 estimated GPP compared to what we find here (e.g see Fares et al., 2019) but do not have an  
614 equivalent in JV.

615

### 616 3.3 Stomatal conductance

617 As the three physiology models in FORCAsT-gs explicitly couple photosynthesis and  
618 stomatal conductance, we now assume that the parameterisation that best represents GPP (as a proxy  
619 for photosynthesis) at each of the sites also best captures fluctuations in stomatal aperture. Figure 5  
620 presents the performance of the models at each site relative to the stomatal conductance or ozone  
621 deposition rate simulated by the best-performing model.

622 The first and second columns of Figure 5 show the average seasonal and diurnal profiles of  
623 stomatal conductance at each site with that estimated by the best performing model shown as a black  
624 line (i.e. assumed as “truth”). The grey shading indicates the full range of stomatal conductance  
625 estimated by the various model configurations.

626 At the tropical site, BR\_Sa1, the BB model, which best captured GPP, is taken to represent  
627 observed stomatal conductance. Stomatal conductance estimated with the model that had the lowest  
628 GPP estimates (JV-) is ~75% lower while the configuration with the greatest overestimation of GPP  
629 (JV+) is ~ 25% higher. The difference between the models remains almost constant throughout the  
630 year at this tropical site. The divergences in stomatal conductance at FI\_Hyy, IT\_Cp2, US\_Blo and  
631 US\_Ha1 are seasonal. For these sites, MD- was used to represent observed  $g_s$  due to its lower  
632 summary statistics shown in Table S4. The difference between the models that over or

633 underestimated GPP were <30% in the winter and spring increasing rapidly to >100% at IT\_Cp2 and  
634 US\_Blo in the summer, and >200% at FI\_Hyy and US\_Ha1.

635 The diel profile of stomatal conductance between the best and worst performing models is  
636 similar to the seasonal profile observed at each site. As shown by the second columns of Figure 5,  
637 BR\_Sa1, IT\_Cp2 and US\_Blo show the widest variation in modelled stomatal conductance between  
638 the different model configurations during peak periods of the day. There is about 10%  
639 overestimation of peak daytime stomatal conductance values at FI\_Hyy and US\_Ha1 between the  
640 best and overestimating model configurations. On the contrary, the models that underestimated GPP  
641 at these sites (JV-) also underestimated stomatal conductance by and >50%.

642

### 643 3.4 Ozone deposition

644 The differences in simulated stomatal conductance between configurations of FORCAsT-gs  
645 affects estimated ozone deposition velocity and hence the rate at which ozone is lost to this key sink.  
646 Figure S6 shows the seasonal and diel profiles of variations in ozone deposition velocity between the  
647 models. The tropical site, BR\_Sa1, and the temperate broadleaf forest, US\_Ha1, have the highest  
648 estimated ozone deposition velocities as expected from their higher  $g_s$ , compared to the other sites.  
649 This higher  $g_s$  and hence ozone deposition velocities are likely due to the fact that plants in these  
650 forests also have bigger leaf sizes and higher leaf area index – highlighting the role of forest structure  
651 and characteristics in plant physiological processes (Meyers & Baldocchi, 1988; Padro, 1996).

652 The deposition velocity is however dependent on several resistances as shown in Eqn. 3,  
653 including the stomatal resistance (the inverse of  $g_s$ ). As a result, the models that overestimated GPP  
654 and  $g_s$  do not necessarily overestimate seasonal deposition velocity when compared to the best  
655 performing model across all sites. However, the model configurations that underestimated GPP and  
656  $g_s$  do underestimate seasonal ozone deposition velocity, although to a lesser extent. For example, JV-  
657 underestimated GPP and  $g_s$  by >100% during the peak growing season but only underestimated

658 deposition velocity by ~15%, with an average value of 0.36 cm s<sup>-1</sup> compared with 0.42 cm s<sup>-1</sup>  
659 estimated with the best performing model (MD). Similarly, at the tropical site, the average deposition  
660 velocity in the optimal model configuration (BB) was 0.88 cm s<sup>-1</sup>. This value was 13% higher than  
661 the average deposition velocity in JV- which underestimated GPP and 6% lower than that of JV+  
662 which overestimated GPP by a factor of 2.

663 The variation between modelled deposition velocities at FI\_Hyy, IT\_Cp2 and US\_Blo  
664 between the model configurations is similar to those described for BR\_Sa1 and US\_Ha1 although the  
665 absolute values are smaller. The only exception here is at IT\_Cp2 where JV+ overestimates  
666 deposition velocity in the summer just as it did for GPP and  $g_s$ . The model divergence in diel profile  
667 of ozone deposition velocity exhibits similar variability to that of the seasonal profile.

668 The seasonal changes in deposition velocity are also very different to that of  $g_s$  at their  
669 respective sites. Ozone deposition velocities at BR\_Sa1, IT\_Cp2 and US\_Ha1, show the greatest  
670 variations, ranging between <5% and ~30% for model configurations that over or underestimated  
671 GPP respectively, relative to the model configuration that produces the best summary statistics for  
672 each site, as defined by Eqn.32 and summarised in Table S4. The two needleleaf forests, FI\_Hyy and  
673 US\_Blo show the least variation in seasonal deposition velocities of <10%.

674 As shown in Eqn. 4, ozone deposition rates depend on ozone concentration as well as  
675 deposition velocity. Hence, while the differences estimated in deposition velocity would be expected  
676 to produce changes in ozone deposition rates at the study sites, they will not be directly proportional.

677 Figure S7 shows average ozone concentrations for each study site for the relevant simulation  
678 time periods. As ozone is produced through photochemical processes concentrations at all sites peak  
679 during the spring and summer and decline steadily in the autumn and winter.

680 Figure 5 shows that the seasonal variation in ozone deposition rate closely follows the  
681 seasonal variation in ozone concentration at all sites. On the contrary, the diel profile of ozone  
682 deposition differs from that of the concentration. While ozone concentrations at all sites peak in the

683 late afternoon or early evening, deposition rates are highest just after midday when  $g_s$  and deposition  
684 velocity are at a maximum. This clearly indicates that deposition velocity, and hence stomatal  
685 conductance, is the key determinant of deposition rates on shorter timescales, while atmospheric  
686 ozone concentrations drive longer temporal trends. The greatest variations in seasonal and diurnal  
687 deposition rates between different model configurations, indicated by the grey shaded areas on  
688 Figure 5, were observed at FI\_Hyy and US\_Ha1, as for the deposition velocities.

689 The diel profile of ozone deposition rates, and their variations due to changes in stomatal  
690 conductance parameterisations, are similar to those of the deposition velocities (Figure S6).  
691 Variations in deposition rates estimated by JV+ which overestimated GPP and stomatal conductance,  
692 and the best-fit models averaged 0.10% - 10% across sites. A 7-13% difference was also seen in the  
693 deposition rates calculated using the best fit and maximal underestimating model configurations.

694 However, the seasonal variations observed in deposition rates are much lower than the  
695 variations in either stomatal conductance or deposition velocity across all sites. There was only ~1%  
696 variation between seasonal ozone deposition rates in model configurations which overestimated GPP  
697 and the best performing model across sites, apart from IT\_Cp2 where deposition rate varied by ~5%  
698 in the summer. Similarly, seasonal deposition rates estimated by model configurations with the  
699 lowest GPP were 7-13% lower than those estimated with the best performing model configurations  
700 (Figure 5). By contrast, modelled stomatal conductance and deposition velocities varied by up to  
701 100% and up to 30% respectively for these same model configurations (Figure 5), confirming the  
702 modulating effect of ozone concentrations.

703 The role of ozone concentrations in determining ozone deposition rates is exemplified at  
704 BR\_Sa1. Average  $g_s$  and deposition velocity were a factor of 2 higher at this site than US\_Ha1 which  
705 had the next highest values. However, the average ozone deposition rates at BR\_Sa1 were  
706 approximately the same as those at US\_Ha1 (0.18 ppb  $\text{cm s}^{-1}$ ). This is due to lower average ozone  
707 concentration at BR\_Sa1 (20 ppb) compared to US\_Ha1 (43 ppb).



## 709 4 Discussion and Conclusion

710 We have found that ozone deposition rates estimated using stomatal conductance simulated  
711 by three of the most widely-used stomatal conductance-photosynthesis models can vary by as much  
712 as 10% depending on ecosystem, season and time of day. As dry deposition is the primary sink for  
713 tropospheric ozone, this has potentially significant implications for estimated ozone budgets across  
714 space and time.

715 By introducing the Jarvis, Ball-Berry and Medlyn parameterisations of stomatal conductance  
716 and photosynthesis into FORCAST1.0, a 1-D column model of trace gas exchange between a forest  
717 canopy and the atmosphere (Ashworth et al. 2015; Otu-Larbi et al., 2020a, 2020b), we were able to  
718 evaluate the performance of the three physiological models via comparison of simulated  
719 photosynthesis with long-term measurements of gross primary productivity (GPP) taken from the  
720 FLUXNET2015 dataset (Pastorello et al., 2020). We find that all three models reproduce the  
721 seasonal and diel variations in GPP well at a range of forest types, Boreal evergreen (FI\_Hyy),  
722 Temperate deciduous (US\_Ha1), and Mediterranean evergreen (IT\_Cp2 and US\_Blo), but struggle  
723 to capture seasonality at a Tropical broadleaf evergreen site (BR\_Sa1).

724 As shown by Figures 2 and 4, the Medlyn stomatal optimisation model provides the best  
725 overall performance at four of the five FLUXNET sites used in this study (FI\_Hyy, IT\_Cp2, US\_Blo  
726 and US\_Ha1), with estimates of GPP within 20%, but is out-performed by the Ball-Berry coupled  
727 stomatal conductance-photosynthesis model at BR\_Sa1. The Ball-Berry model also successfully  
728 captures GPP across all sites, with divergence from observation mostly <10% except for the drought-  
729 prone Mediterranean IT\_Cp2 site, at which modelled GPP is 15-20% higher than observed GPP  
730 during the middle of the day. The superior performance of MD compared to BB at this site could be  
731 expected as MD was specifically developed as an improvement on BB to optimise carbon gain while  
732 limiting water loss (Medlyn et al., 2011). Except for US\_Blo, where JV reproduced the observed

733 annual and diel profiles of GPP to within 20%, the Jarvis multiplicative model either substantially  
734 overestimated or underestimated GPP, by as much as a factor of 2. The relatively poor performance  
735 of JV in reproducing observed GPP is perhaps not surprising since photosynthesis estimates are  
736 based on a simple assumption of a linear relationship between stomatal conductance and carbon  
737 assimilation (Eqn.6).

738         The superior performance of the Medlyn optimisation model in the two Mediterranean  
739 climates could also be due to the fact that vegetation response to soil moisture stress is better  
740 accounted for through a combination of stomatal and biochemical limitations (e.g. see De Kauwe et  
741 al., 2015; Lin et al., 2015; Otu-Larbi et al., 2020). BB, by comparison, assumes that drought stress  
742 directly downregulates photosynthesis rates or is the result of biochemical limitation only (e.g see  
743 Best et al., 2011; Clark et al., 2011; Fares et al., 2019). This finding is supported by previous work  
744 which shows that the choice of drought stress parameterisation is an important factor that determines  
745 model performance in a water stressed environment (Egea et al.,2011; Keenan et al., 2010).

746         The poor performance of the models at the tropical evergreen site (BR\_Sa1) is likely due to  
747 the assumption of a uniform forest structure for this evergreen forest site throughout the year.  
748 Subsequently,  $f_{phen}$  in JV (Eqn. 5) is set to a value of 1 and constant LAI is used in estimating  
749 photosynthetic capacity in BB and MD models. A modelling study by Flack-Prain et al. (2019)  
750 indicates that changes in LAI could account for up to 33% of observed variations in Amazonian  
751 forest GPP. This suggests the need for an improved understanding of changes in forest structure and  
752 phenology in tropical ecosystems to obtain more accurate model estimation of GPP at this and other  
753 tropical sites (Rödig et al., 2018). In addition, photosynthetic rates and stomatal conductance are  
754 controlled by solar radiation and temperature and limited by stress factors like drought and air  
755 pollutants including ozone (Nemani et al., 2003). For BR\_Sa1, both temperature and PAR (Figure 1a  
756 and b; orange lines) remain fairly constant throughout the year which would lead to higher modelled  
757 photosynthetic capacity in BB and MD since modelled  $V_{cmax}$  and  $J_{max}$  are reliant on temperature.

758 Seasonal variations in  $V_{cmax}$  and  $J_{max}$  are reported to be a major source of uncertainty in GPP estimates  
759 in Amazonian forests (Flack-Prain et al., 2019). It is worth noting that US\_Blo and IT\_Cp2 which  
760 are also evergreen forest were treated similarly, but as shown in Figures 2 and 4, the models  
761 performed better at this site, perhaps due to a compensating error in modelling drought stress.

762 Results from sensitivity tests conducted on key stomatal conductance parameters in JV, BB  
763 and MD models revealed that modelled GPP and stomatal conductance values are highly sensitive to  
764 the choice of conductance parameters. Variations of ~5-75% from base model estimates were  
765 observed in modelled GPP and stomatal conductance in response to ~10-60% variation in model  
766 parameters. Such wide differences could reduce the reliability of estimated reductions in crop or  
767 plant productivity due to air pollutants such as ozone.

768 The findings from this study make it imperative that more measurements of these key  
769 conductance parameters are made to improve understanding and model representation of dry  
770 deposition. The Jarvis model showed greater sensitivity to choice of parameter value than either  
771 Ball-Berry or Medlyn. It must be noted that the Jarvis parameter  $g_{max}$  is typically measured in sunlit  
772 leaves at the top of the canopy. Leaves below the canopy often differ in their shape and leaf angle  
773 classes from those at the top of the canopy (Niinemets, 2010). The JV model as implemented in  
774 FORCAsT and elsewhere assumes the same  $g_{max}$  for all angle classes and model levels. More work is  
775 needed to improve the parameterisation of variations in  $g_{max}$  for different levels in the canopy and leaf  
776 angle classes.

777 We conclude that the Medlyn coupled stomatal conductance-photosynthesis model would be  
778 the best default selection. However, our model simulations also point to the need for improved  
779 stomatal conductance-photosynthesis model parameterisations for tropical ecosystems where  
780 seasonality is driven by contrasts in precipitation rather than temperature and solar radiation.

781 We tested the response of ozone deposition rate at different ecosystems to changes in  
782 stomatal conductance parameterisations while keeping model calculations of other resistances

783 unchanged. The choice of stomatal conductance model parameters was found to be a very important  
784 factor in determining ozone deposition rates across all sites. Seasonal and daily deposition rates to  
785 the forest canopy changed by as much as 13% with implications for air quality modelling and  
786 assessment of ozone damage to crops and plants. Most models used in assessing air quality at global,  
787 regional, and local levels consider dry deposition using variants of the same Wesely deposition  
788 scheme used in FORCAST-gs (Hardacre et al., 2015). Many international assessments of ozone  
789 damage to crops and forests are based on dose-response parameters developed using the JV model  
790 (e.g. see Emberson et al., 2000, Hayes et al., 2007; Mills et al., 2011; Buker et al., 2015). Like air  
791 quality models, dose-response relationships rely on ozone deposition rates and their accuracy and  
792 reliability could be severely diminished if the appropriate model parameterisations are not used.  
793 Large uncertainty in modelled deposition rates due to the choice of model parameters, as found in  
794 this study, could therefore affect modelled surface ozone concentrations with negative implications  
795 for air quality monitoring as well as assessments of plant productivity losses from ozone damage.  
796 This is especially true for models that rely on the Jarvis multiplicative model to estimate stomatal  
797 conductance. Our results highlight the need for models to carefully consider the choice of model  
798 parameters as this will ultimately determine model performance.

799         Similar to other studies, we found the highest stomatal conductance and ozone deposition  
800 velocities at tropical and broadleaf forest site compared to needleleaf and coniferous forests (e.g. see  
801 Emberson et al., 2001; Fowler et al., 2001; 2011; Kumar et al., 2011; Silva & Heald, 2018). The  
802 larger LAI at the broadleaf forests (BR\_Sa1 and US\_Ha1), leads to greater canopy conductance,  
803 lower stomatal resistance, and subsequently higher deposition velocity as these are important for  
804 estimating total canopy and leaf boundary resistance (Meyers & Baldocchi, 1988; Padro, 1996).  
805 Ozone deposition velocities at BR\_Sa1 were up to a factor of three higher than those at IT\_Cp2,  
806 US\_Blo and FI\_Hyy. However, the difference in ozone deposition rates were much lower (<30%)  
807 due to lower ozone concentrations at this remote forest site.

808 Our findings of the sensitivity of stomatal conductance estimates to parameter and algorithm  
809 choice could also have important implications in modelling biogenic volatile organic compound  
810 (BVOC) emissions. Current BVOC emission models rely on leaf temperature and solar radiation to  
811 drive emission rates and are known to reproduce observations for a range of forest ecosystems and  
812 climates within a factor of two (e.g. see Guenther et al., 1993; 1995; 2006). However, such models  
813 have been shown to struggle to reproduce diurnal emission patterns of short-chained carboxylic  
814 acids and aldehydes, leading to suggestions that the failure to include stomatal conductance in such  
815 models could be a limiting factor in model performance (Kesselmeier et al., 1997; Martin et al.,  
816 1999; Staudt et al., 2000; Niinemets and Reichstein, 2003). Including stomatal control of emission  
817 rates in land-atmosphere models would need to account for the sensitivity of simulated stomatal  
818 conductance to the choice of physiological model.

819

820

821 **Code availability**

822 FORCAST-gs is available for download on request to the corresponding author.

823 **Data availability**

824 FLUXNET2015 data for BR\_Sa1, FI\_Hyy, IT\_Cp2, US\_Blo, and US\_Ha1 can all be  
825 accessed and downloaded from <https://fluxnet.fluxdata.org/data/fluxnet2015-dataset/>; the doi of each  
826 dataset is shown in Table 1.

827

828 **Author contribution**

829 All co-authors were involved in conceptualization of the research and writing of the manuscript. F.  
830 Otu-Larbi and K. Ashworth performed model simulations and analysed results.

831

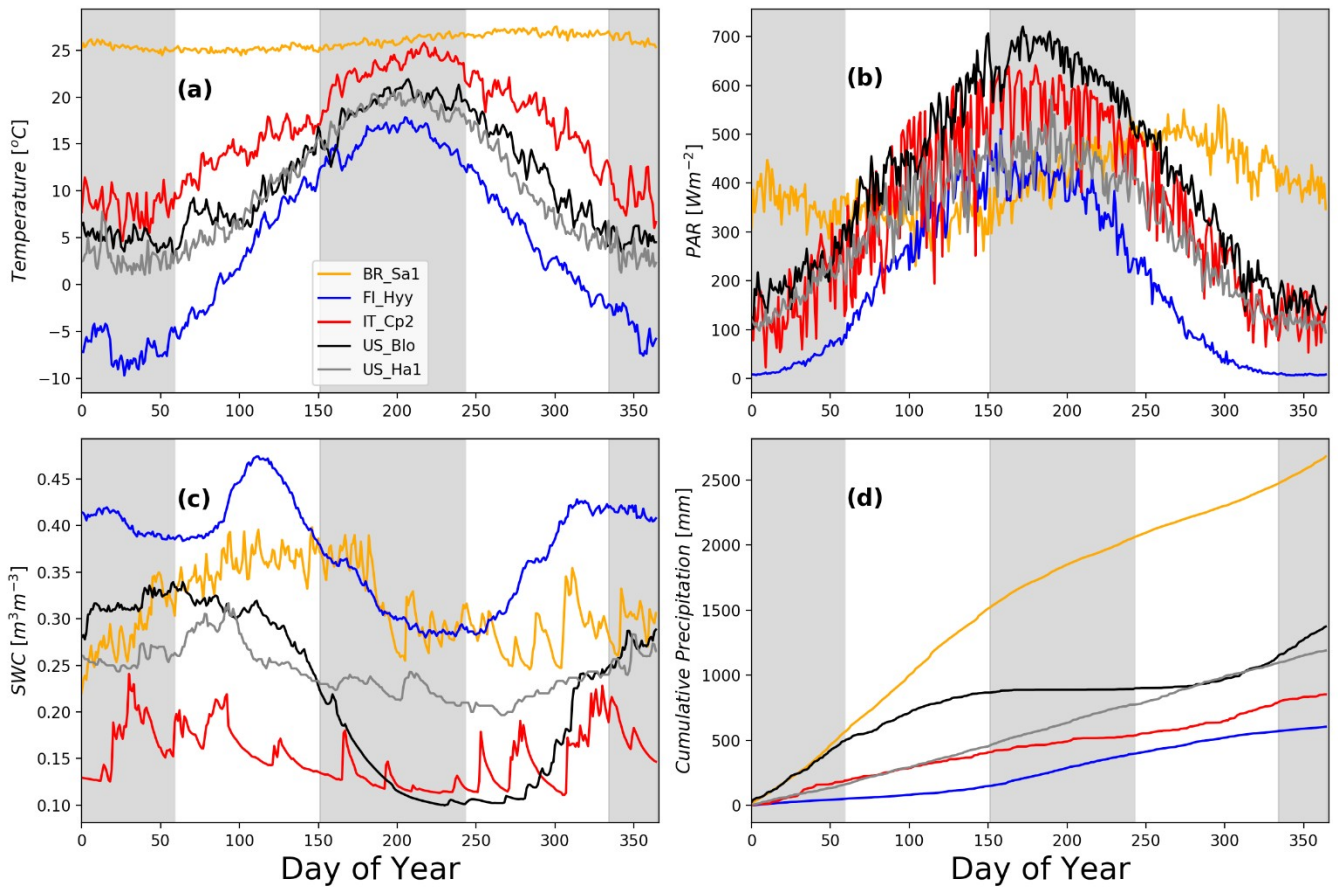
832 **Competing interests**

833 The authors declare no competing interests.

834 **Acknowledgements**

835 F. Otu-Larbi is grateful to the Faculty of Science and Technology (FST) and Lancaster  
836 Environment Centre (LEC) at Lancaster University for funding his PhD Studentship. K. Ashworth is  
837 a Royal Society Dorothy Hodgkin Fellow and thanks the Royal Society of London for their support  
838 and funding (DH150070). The authors are grateful to the FLUXNET network, and specifically the  
839 lead investigators at each of the study sites, for the ready availability of all data collected at these  
840 sites.

841



842

843 Figure 1: Site conditions and meteorology showing (a) soil moisture (volumetric soil water content,  
 844 SWC;  $m^3 m^{-3}$ ); (b) cumulative precipitation (mm); (c) 2-m air temperature ( $^{\circ}C$ ) and (d)  
 845 photosynthetically active radiation (PAR) at the top of the canopy ( $W m^{-2}$ ) for an average year at  
 846 BR\_Sa1 (yellow), FI\_Hyy (blue), IT\_Cp2 (red), US\_Blo (black) and US\_Ha1 (grey)  
 847

848

849

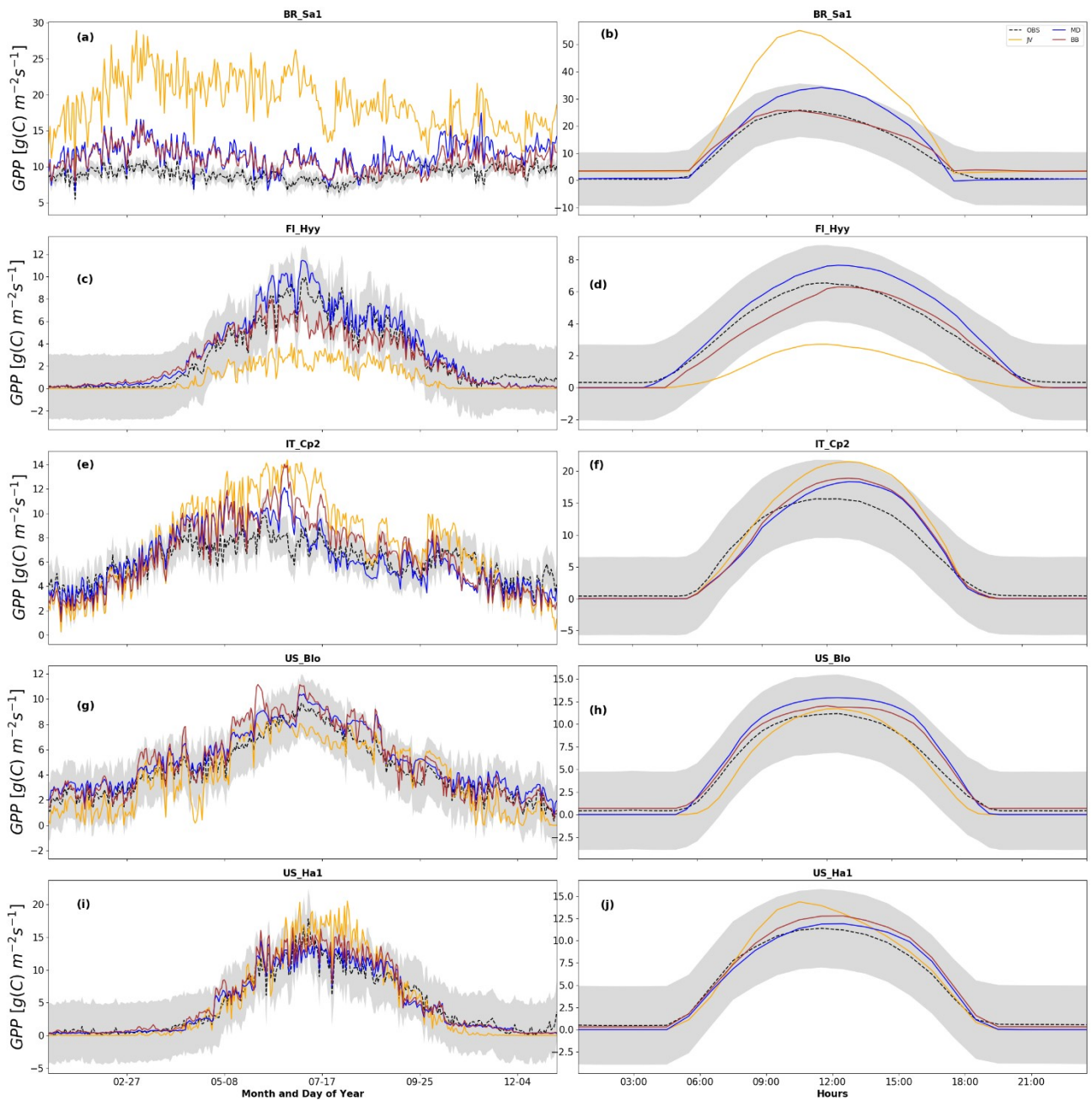
850

851

852

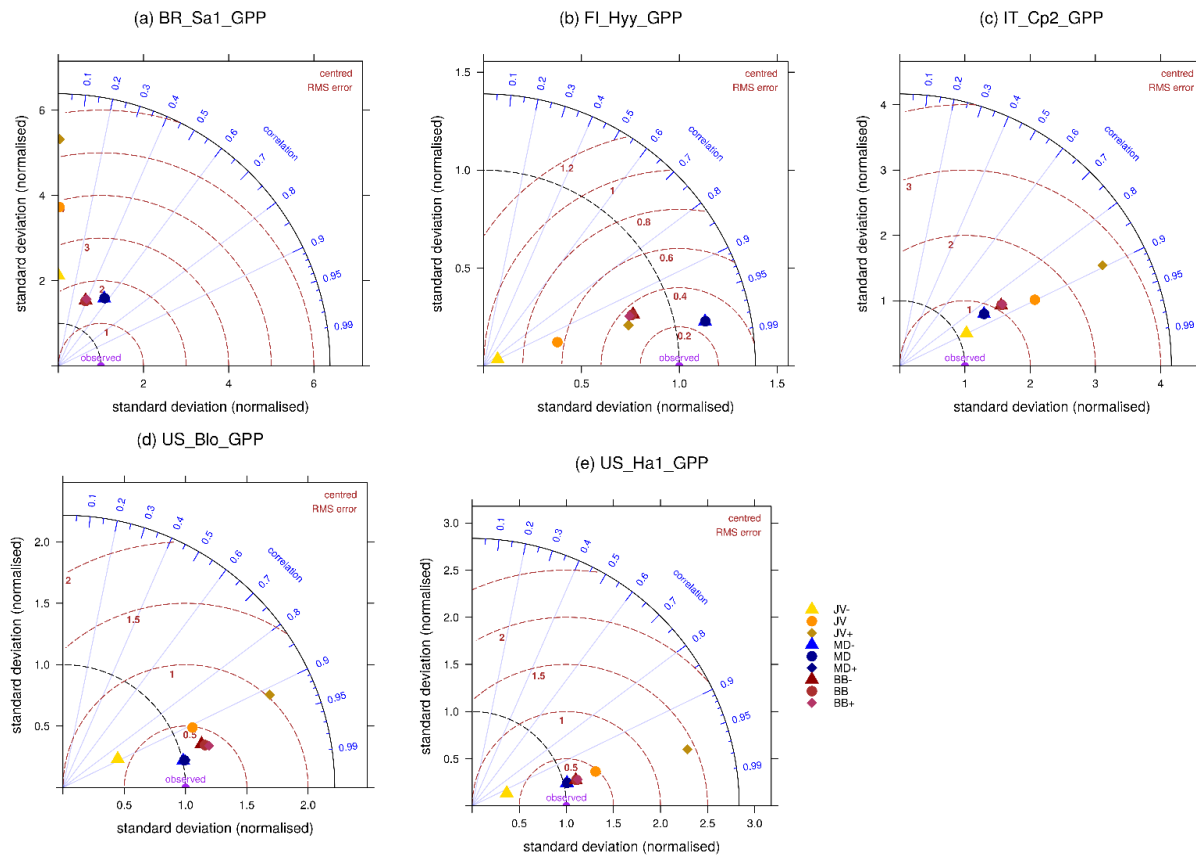
853

854



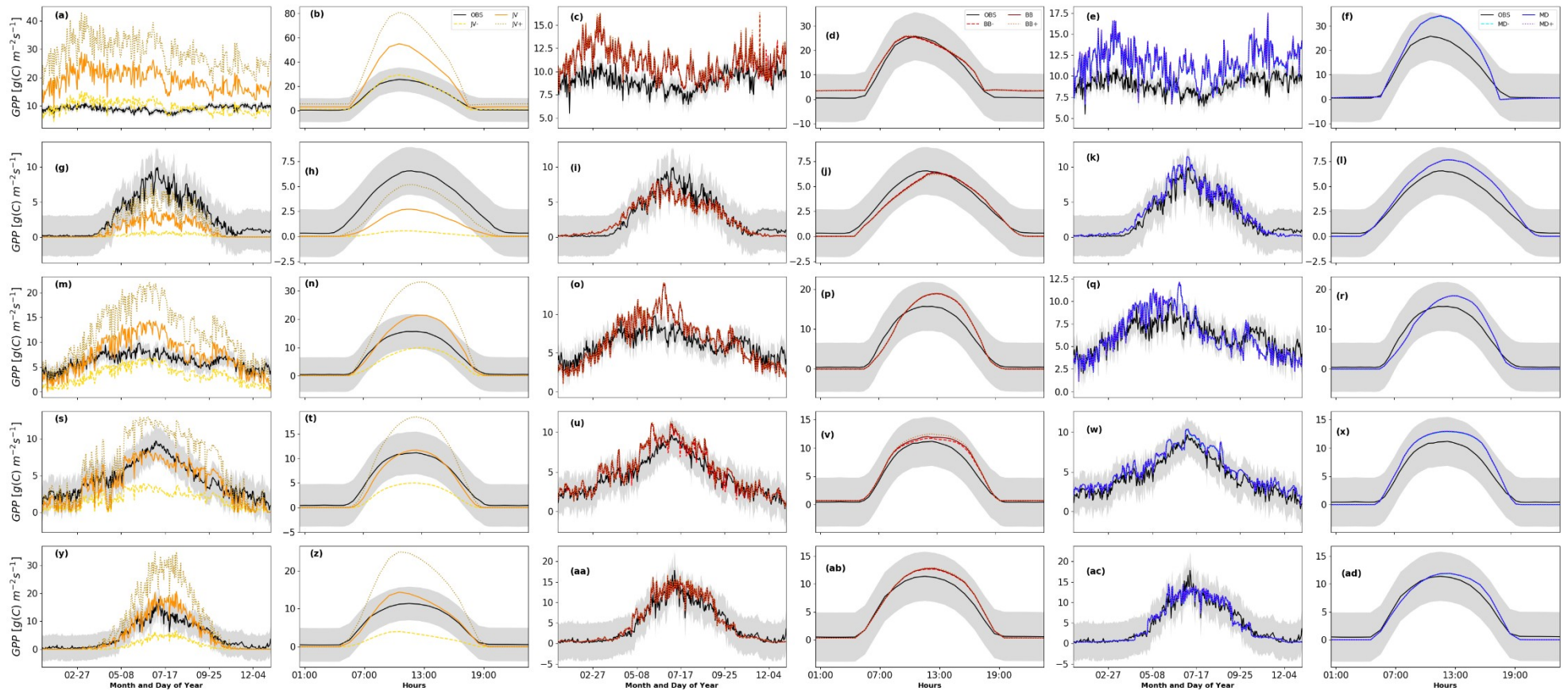
855

856 Figure 2: Net photosynthesis for an average year at each of the five FLUXNET sites, from top to  
 857 bottom: BR\_Sa1, FI\_Hyy, IT\_Cp2, US\_Blo, US\_Ha1. The first column shows average annual and  
 858 the second average diel profiles of Gross Primary Productivity (GPP, a measure of photosynthesis  
 859 rate) estimated from the Jarvis multiplicative (gold), Ball-Berry coupled (red) and Medlyn stomatal  
 860 optimisation coupled (blue) stomatal conductance-photosynthesis models. The black dashed lines  
 861 show observed GPP.



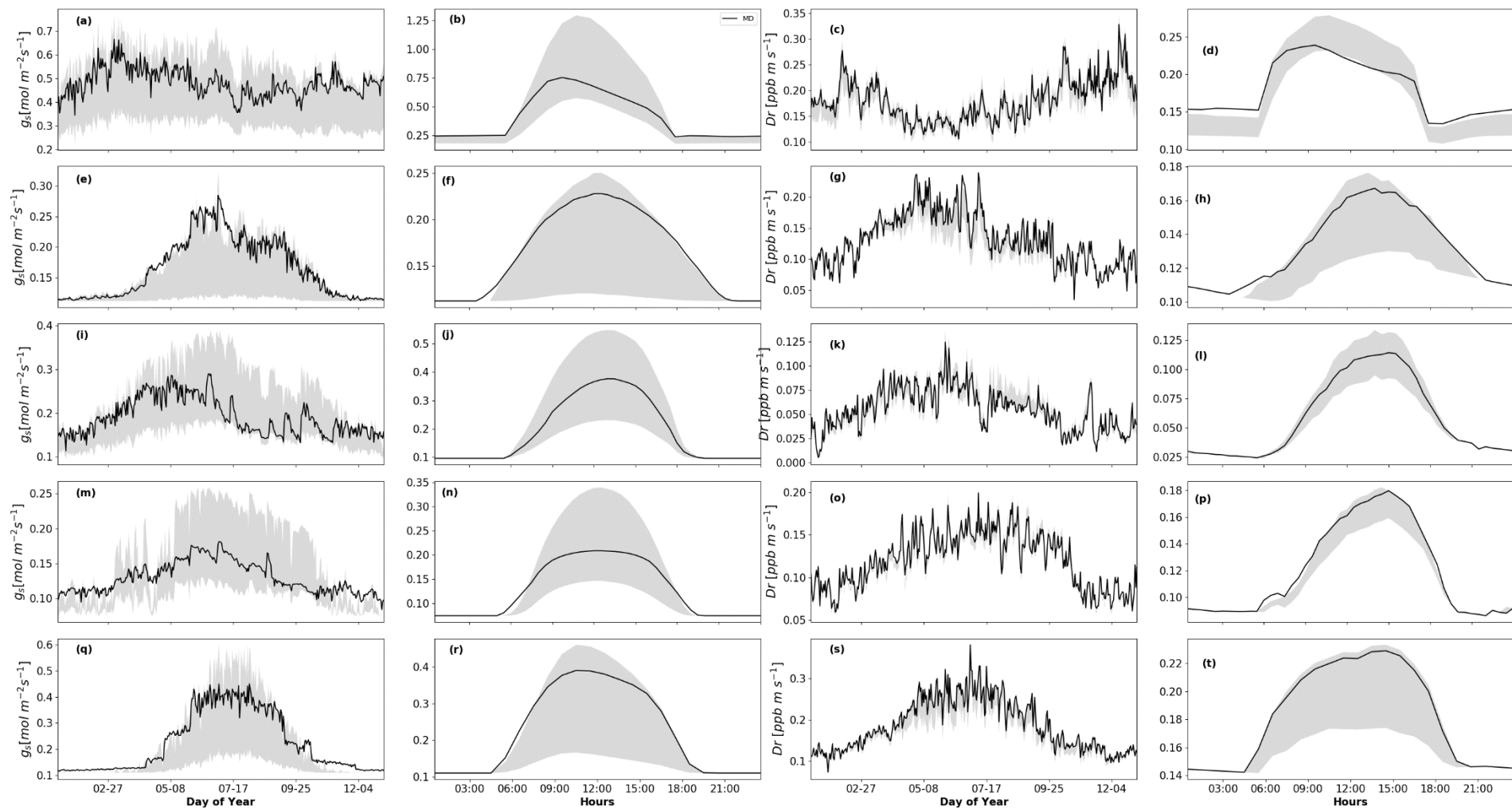
862

863 Figure 3: Taylor Diagram summarising model output statistics from FORCAsT sensitivity tests. Observed GPP has SD=1.0, RMSE=0.0 and  $r=1.0$   
 864 (purple circle). Black and brown dashed curves and blue lines show normalised standard deviation (SD), centred root mean squared error (RMSE) and  
 865 correlation coefficients ( $r$ ) respectively against observations for each model on each diagram. The summary statistics for each JV simulation are shown  
 866 by gold symbols, BB by red, MD simulation by blue. BASE simulations are denoted by circles, lower bounds (TEST-) by triangles, and upper bounds  
 867 (TEST+) by diamonds. Note that JV, MD and BB in these plots are the BASE simulations described in sections 2.5.1 and 3.1, and Figure 2.



868

869 Figure 4: Gas exchange for an average year at each of the five FLUXNET sites, from top to bottom: BR\_Sa1, FI\_Hyy, IT\_Cp2, US\_Blo, US\_Ha1, for,  
 870 from left to right, the Jarvis, Ball-Berry and Medlyn stomatal conductance model sensitivity tests. Solid lines denote the unperturbed (BASE) simulation  
 871 as shown in Figure 2 for each model, with dashed paler line for TEST- and dashed darker line for TEST+ simulations respectively. The black dashed  
 872 lines show observed GPP at each site.



873

874 Figure 5: Stomatal conductance and ozone deposition rates for an average year and day at each of the five FLUXNET sites, from top to bottom:  
 875 BR\_Sa1, FI\_Hyy, IT\_Cp2, US\_Blo, and US\_Ha1. Solid lines black lines denote the output from the model that best reproduced GPP at each site as  
 876 shown in Figure 3 and 4. The shaded regions indicate the spread in stomatal conductance and deposition rates across all the model sensitivity tests.

877 **References**

878

879 Ainsworth, E. A., Yendrek, C. R., Sitch, S., Collins, W. J., & Emberson, L. D. (2012).  
880 The effects of tropospheric O<sub>3</sub> on net primary productivity and implications for  
881 climate change. *Annual Review of Plant Biology*, 63, 637– 661.  
882 <https://doi.org/10.1146/annurev-arplant-042110-103829>

883 Allen, A. (1995). Soil science and survey at Harvard Forest. *Soil survey horizons*,  
884 36(4), 133-142. <https://doi.org/10.2136/sh1995.4.0133>

885 Ashworth, K., Chung, S. H., Griffin, R. J., Chen, J., Forkel, R., Bryan, A. M., &  
886 Steiner, A. L. (2015). FORest Canopy Atmosphere Transfer (FORCAsT) 1.0: A 1-D  
887 model of biosphere-atmosphere chemical exchange. *Geoscientific Model*  
888 *Development*, 8(11), 3765– 3784. <https://doi.org/10.5194/gmd-8-3765-2015>

889 Avnery, S., Mauzerall, D. L., Liu, J., & Horowitz, L. W. (2011). Global crop yield  
890 reductions due to surface ozone exposure: 1. Year 2000 crop production losses and  
891 economic damage. *Atmospheric Environment*, 45(13), 2284-  
892 2296. <https://doi.org/10.1016/j.atmosenv.2010.11.045>

893 Baldocchi, D. (1988). A multi-layer model for estimating sulfur dioxide deposition to  
894 a deciduous oak forest canopy. *Atmospheric Environment*  
895 22. [https://doi.org/10.1016/0004-6981\(88\)90264-8](https://doi.org/10.1016/0004-6981(88)90264-8)

896 Baldocchi, D. (1994). An analytical solution for coupled leaf photosynthesis and  
897 stomatal conductance models. *Tree physiology*, 14(7-8-9),  
898 1069-1079. <https://doi.org/10.1093/treephys/14.7-8-9.1069>

899 Ball, J. T., Woodrow, I. E., & Berry, J. A. (1987). A model predicting stomatal  
900 conductance and its contribution to the control of photosynthesis under different

901 environmental conditions. In Progress in photosynthesis research (pp. 221-224).  
902 Springer, Dordrecht.

903 Best, M. J., Pryor, M., Clark, D. B., Rooney, G. G., Essery, R., Ménard, C. B., ... &  
904 Harding, R. J. (2011). The Joint UK Land Environment Simulator (JULES), model  
905 description–Part 1: energy and water fluxes. *Geoscientific Model Development*, 4(3),  
906 677-699. <https://doi.org/10.5194/gmd-4-677-2011>

907 Blackadar, A. K. (1962). The vertical distribution of wind and turbulent exchange in a  
908 neutral atmosphere. *Journal of Geophysical Research*, 67(8),  
909 3095-3102. <https://doi.org/10.1029/JZ067i008p03095>

910 Bryan, A. M., Bertman, S. B., Carroll, M. A., Dusanter, S., Edwards, G. D., Forkel,  
911 R., ... & Steiner, A. L. (2012). In-canopy gas-phase chemistry during CABINEX  
912 2009: sensitivity of a 1-D canopy model to vertical mixing and isoprene chemistry.  
913 *Atmospheric Chemistry and Physics*, 12(18), 8829-8849. [https://doi.org/10.5194/acp-](https://doi.org/10.5194/acp-12-8829-2012)  
914 [12-8829-2012](https://doi.org/10.5194/acp-12-8829-2012)

915 Bryan, A. M., Cheng, S. J., Ashworth, K., Guenther, A. B., Hardiman, B. S., Bohrer,  
916 G., & Steiner, A. L. (2015). Forest-atmosphere BVOC exchange in diverse and  
917 structurally complex canopies: 1-D modeling of a mid-successional forest in northern  
918 Michigan. *Atmospheric Environment*, 120,  
919 217-226. <https://doi.org/10.1016/j.atmosenv.2015.08.094>

920 Büker, P., Feng, Z., Uddling, J., Briolat, A., Alonso, R., Braun, S., ... & Emberson, L.  
921 D. (2015). New flux based dose–response relationships for ozone for European forest  
922 tree species. *Environmental Pollution*, 206, 163-174.  
923 <https://doi.org/10.1016/j.envpol.2015.06.033>

924 Büker, P., Feng, Z., Uddling, J., Briolat, A., Alonso, R., Braun, S., ... & Emberson, L.  
925 D. (2015). New flux based dose–response relationships for ozone for European forest

926 tree species. *Environmental Pollution*, 206, 163-174.  
927 <https://doi.org/10.1016/j.envpol.2015.06.033>

928 Chen, J., Mao, H., Talbot, R. W., & Griffin, R. J. (2006). Application of the CACM  
929 and MPMPO modules using the CMAQ model for the eastern United States. *Journal*  
930 *of Geophysical Research: Atmospheres*, 111(D23).  
931 <https://doi.org/10.1029/2006JD007603>

932 Clark, D. B., Mercado, L. M., Sitch, S., Jones, C. D., Gedney, N., Best, M. J., ... Cox,  
933 P. M. (2011). The Joint UK Land Environment Simulator (JULES), model description  
934 – Part 2: Carbon fluxes and vegetation dynamics. *Geoscientific Model Development*,  
935 4(3), 701–722. <https://doi.org/10.5194/gmd-4-701-2011>

936 Clifton, O. E., Fiore, A. M., Munger, J. W., & Wehr, R. (2019). Spatiotemporal  
937 controls on observed daytime ozone deposition velocity over northeastern US forests  
938 during summer. *Journal of Geophysical Research: Atmospheres*, 124(10), 5612-5628.  
939 <https://doi.org/10.1029/2018JD029073>

940 Cowan, I. R., & GD, Farquhar, G.D. (1977). Stomatal function in relation to leaf  
941 metabolism and environment.

942 Da Rocha, H. R., Goulden, M. L., Miller, S. D., Menton, M. C., Pinto, L. D., de  
943 Freitas, H. C., & e Silva Figueira, A. M. (2004). Seasonality of water and heat fluxes  
944 over a tropical forest in eastern Amazonia. *Ecological applications*, 14(sp4), 22-32.  
945 <https://doi.org/10.1890/02-6001>

946 Damour, G., Simonneau, T., Cochard, H., & Urban, L. (2010). An overview of models  
947 of stomatal conductance at the leaf level. *Plant, cell & environment*, 33(9), 1419-  
948 1438. <https://doi.org/10.1111/j.1365-3040.2010.02181.x>

949 De Kauwe, M. G., Kala, J., Lin, Y. S., Pitman, A. J., Medlyn, B. E., Duursma, R.  
950 A., ... & Miralles, D. G. (2015). A test of an optimal stomatal conductance scheme

951 within the CABLE land surface model. *Geoscientific Model Development*, 8(2), 431-  
952 452. <https://doi.org/10.5194/gmd-8-431-2015>

953 Egea, G., Verhoef, A., & Vidale, P. L. (2011). Towards an improved and more  
954 flexible representation of water stress in coupled photosynthesis–stomatal  
955 conductance models. *Agricultural and Forest Meteorology*, 151(10), 1370– 1384.  
956 <https://doi.org/10.1016/j.agrformet.2011.05.019>

957 Emberson, L. D., Ashmore, M. R., Simpson, D., Tuovinen, J. P., & Cambridge, H. M.  
958 (2001). Modelling and mapping ozone deposition in Europe. *Water, Air, and Soil*  
959 *Pollution*, 130(1), 577-582. <https://doi.org/10.1023/A:1013851116524>

960 Fares, S., Alivernini, A., Conte, A., & Maggi, F. (2019). O<sub>3</sub> and particle fluxes in a  
961 Mediterranean forest predicted by the AIRTREE model. *Science of the Total*  
962 *Environment*, 682, 494– 504. <https://doi.org/10.1016/j.scitotenv.2019.05.109>

963 Fares, S., Matteucci, G., Mugnozza, G. S., Morani, A., Calfapietra, C., Salvatori, E., ...  
964 & Loreto, F. (2013). Testing of models of stomatal ozone fluxes with field  
965 measurements in a mixed Mediterranean forest. *Atmospheric environment*, 67, 242-  
966 251. <https://doi.org/10.1016/j.atmosenv.2012.11.007>

967 Fares, S., Mereu, S., Scarascia Mugnozza, G., Vitale, M., Manes, F., Frattoni, M., ...  
968 & Loreto, F. (2009). The ACCENT-VOCBAS field campaign on biosphere-  
969 atmosphere interactions in a Mediterranean ecosystem of Castelporziano (Rome): site  
970 characteristics, climatic and meteorological conditions, and eco-physiology of  
971 vegetation. *Biogeosciences*, 6(6), 1043-1058. <https://doi.org/10.5194/bg-6-1043-2009>

972 Farquhar, G. D., & Von Caemmerer, S. (1982). Modelling of photosynthetic response  
973 to environmental conditions. In *Physiological plant ecology II* (pp. 549-587).  
974 Springer, Berlin, Heidelberg.

975 Farquhar, G. D., von Caemmerer, S. V., & Berry, J. A. (1980). A biochemical model  
976 of photosynthetic CO<sub>2</sub> assimilation in leaves of C<sub>3</sub> species. *Planta*, 149(1), 78-90.  
977 <https://doi.org/10.1007/BF00386231>

978 Flack-Prain, S., Meir, P., Malhi, Y., Smallman, T. L., & Williams, M. (2019). The  
979 importance of physiological, structural and trait responses to drought stress in driving  
980 spatial and temporal variation in GPP across Amazon forests. *Biogeosciences*, 16(22),  
981 4463-4484. <https://doi.org/10.5194/bg-16-4463-2019>

982 Forkel, R., Klemm, O., Graus, M., Rappenglück, B., Stockwell, W. R., Grabmer,  
983 W., ... & Steinbrecher, R. (2006). Trace gas exchange and gas phase chemistry in a  
984 Norway spruce forest: A study with a coupled 1-dimensional canopy atmospheric  
985 chemistry emission model. *Atmospheric environment*, 40, 28-42.  
986 <https://doi.org/10.1016/j.atmosenv.2005.11.070>

987 Fowler, D., Flechard, C., Cape, J. N., Storeton-West, R. L., & Coyle, M. (2001).  
988 Measurements of ozone deposition to vegetation quantifying the flux, the stomatal and  
989 non-stomatal components. *Water, Air, and Soil Pollution*, 130(1), 63-74.  
990 <https://doi.org/10.1023/A:1012243317471>

991 Fowler, D., Nemitz, E., Misztal, P., Di Marco, C., Skiba, U., Ryder, J., ... & Hewitt, C.  
992 N. (2011). Effects of land use on surface-atmosphere exchanges of trace gases and  
993 energy in Borneo: comparing fluxes over oil palm plantations and a  
994 rainforest. *Philosophical Transactions of the Royal Society B: Biological*  
995 *Sciences*, 366(1582), 3196-3209. <https://doi.org/10.1098/rstb.2011.0055>

996 Fusaro, L., Salvatori, E., Mereu, S., Silli, V., Bernardini, A., Tinelli, A., & Manes, F.  
997 (2015). Researches in Castelporziano test site: ecophysiological studies on  
998 Mediterranean vegetation in a changing environment. *Rendiconti Lincei*, 26(3), 473-  
999 481. <https://doi.org/10.1007/s12210-014-0374-1>

1000 Gao, W., Wesely, M. L., & Doskey, P. V. (1993). Numerical modeling of the  
1001 turbulent diffusion and chemistry of NO<sub>x</sub>, O<sub>3</sub>, isoprene, and other reactive trace  
1002 gases in and above a forest canopy. *Journal of Geophysical Research: Atmospheres*,  
1003 98(D10), 18339-18353. <https://doi.org/10.1029/93JD01862>

1004 Gao, Y., Markkanen, T., Thum, T., Aurela, M., Lohila, A., Mammarella, I., ... Aalto,  
1005 T. (2016). Assessing various drought indicators in representing summer drought in  
1006 boreal forests in Finland. *Hydrology and Earth System Sciences*, 20, 175– 191. [https://](https://doi.org/10.5194/hess-20-175-2016)  
1007 [doi.org/10.5194/hess-20-175-2016](https://doi.org/10.5194/hess-20-175-2016)

1008 Geiger, H., Barnes, I., Bejan, I., Benter, T., & Spittler, M. (2003). The tropospheric  
1009 degradation of isoprene: an updated module for the regional atmospheric chemistry  
1010 mechanism. *Atmospheric Environment*, 37(11),  
1011 1503-1519. [https://doi.org/10.1016/S1352-2310\(02\)01047-6](https://doi.org/10.1016/S1352-2310(02)01047-6)

1012 Goldstein, A. H., & Schade, G. W. (2000). Quantifying biogenic and anthropogenic  
1013 contributions to acetone mixing ratios in a rural environment. *Atmospheric*  
1014 *Environment*, 34(29-30), 4997-5006. [https://doi.org/10.1016/S1352-2310\(00\)00321-6](https://doi.org/10.1016/S1352-2310(00)00321-6)

1015 Goldstein, A. H., Goulden, M. L., Munger, J. W., Wofsy, S. C., & Geron, C. D.  
1016 (1998). Seasonal course of isoprene emissions from a midlatitude deciduous forest.  
1017 *Journal of Geophysical Research: Atmospheres*, 103(D23),  
1018 31045-31056. <https://doi.org/10.1029/98JD02708>

1019 Goldstein, A. H., Hultman, N. E., Fracheboud, J. M., Bauer, M. R., Panek, J. A., Xu,  
1020 M., ... & Baugh, W. (2000). Effects of climate variability on the carbon dioxide,  
1021 water, and sensible heat fluxes above a ponderosa pine plantation in the Sierra Nevada  
1022 (CA). *Agricultural and Forest Meteorology*, 101(2-3), 113-129.  
1023 [https://doi.org/10.1016/S0168-1923\(99\)00168-9](https://doi.org/10.1016/S0168-1923(99)00168-9)

1024 Goulden, M. L., Miller, S. D., Da Rocha, H. R., Menton, M. C., de Freitas, H. C., e  
1025 Silva Figueira, A. M., & de Sousa, C. A. D. (2004). Diel and seasonal patterns of  
1026 tropical forest CO<sub>2</sub> exchange. *Ecological Applications*, 14(sp4), 42-54. [https://doi.org/](https://doi.org/10.1890/02-6008)  
1027 10.1890/02-6008

1028 Griffin, R. J., Dabdub, D., & Seinfeld, J. H. (2005). Development and initial  
1029 evaluation of a dynamic species-resolved model for gas phase chemistry and size-  
1030 resolved gas/particle partitioning associated with secondary organic aerosol  
1031 formation. *Journal of Geophysical Research: Atmospheres*, 110(D5).  
1032 <https://doi.org/10.1029/2004JD005219>

1033 Griffin, R. J., Nguyen, K., Dabdub, D., & Seinfeld, J. H. (2003). A coupled  
1034 hydrophobic-hydrophilic model for predicting secondary organic aerosol formation.  
1035 *Journal of Atmospheric Chemistry*, 44(2), 171-190.  
1036 <https://doi.org/10.1023/A:1022436813699>

1037 Griffin, R. J., Nguyen, K., Dabdub, D., & Seinfeld, J. H. (2003). A coupled  
1038 hydrophobic-hydrophilic model for predicting secondary organic aerosol  
1039 formation. *Journal of Atmospheric Chemistry*, 44(2), 171-190. [https://doi.org/10.1023/](https://doi.org/10.1023/A:1022436813699)  
1040 A:1022436813699

1041 Guenther, A., Hewitt, C. N., Erickson, D., Fall, R., Geron, C., Graedel, T., ... Pierce,  
1042 T. (1995). A global model of natural volatile organic compound emissions. *Journal of*  
1043 *Geophysical Research: Atmospheres*, 100(D5), 8873– 8892.  
1044 <https://doi.org/10.1029/94JD02950>.

1045 Guenther, A., Karl, T., Harley, P., Wiedinmyer, C., Palmer, P. I., & Geron, C. (2006).  
1046 Estimates of global terrestrial isoprene emissions using MEGAN (Model of Emissions  
1047 of Gases and Aerosols from Nature). *Atmospheric Chemistry and Physics*, 6(11),  
1048 3181– 3210. <https://doi.org/10.5194/acp-6-3181-2006>

1049 Guenther, A., Zimmerman, P. R., Harley, P. C., Monson, R. K., & Fall, R. (1993).  
1050 Isoprene and monoterpene emission rate variability: Model evaluations and sensitivity  
1051 analyses. *Journal of Geophysical Research*, 98(D7), 12609.  
1052 <https://doi.org/10.1029/93JD00527>

1053 Hardacre, C., Wild, O., & Emberson, L. (2015). An evaluation of ozone dry  
1054 deposition in global scale chemistry climate models. *Atmospheric Chemistry and*  
1055 *Physics*, 15(11), 6419-6436. <https://doi.org/10.5194/acp-15-6419-2015>

1056 Hari, P., & Kulmala, M. (2005). Station for Measuring Ecosystem Atmosphere  
1057 Relations (SMEAR II). *Boreal Environmental Research*, 10, 315– 322.

1058 Harley, P. C., Thomas, R. B., Reynolds, J. F., & Strain, B. R. (1992). Modelling  
1059 photosynthesis of cotton grown in elevated CO<sub>2</sub>. *Plant, Cell & Environment*, 15(3),  
1060 271-282. <https://doi.org/10.1111/j.1365-3040.1992.tb00974.x>

1061 Hayes, F., Mills, G., Harmens, H., & Norris, D. (2007). Evidence of widespread ozone  
1062 damage to vegetation in Europe (1990-2006). ICP Vegetation Programme  
1063 Coordination Centre, CEH Bangor, UK.

1064 Hetherington, A. M., & Woodward, F. I. (2003). The role of stomata in sensing and  
1065 driving environmental change. *Nature*, 424(6951),  
1066 901-908. <https://doi.org/10.1038/nature01843>

1067 Hoshika, Y., Osada, Y., De Marco, A., Penuelas, J., & Paoletti, E. (2018). Global  
1068 diurnal and nocturnal parameters of stomatal conductance in woody plants and major  
1069 crops. *Global Ecology and Biogeography*, 27(2), 257-275.  
1070 **<https://doi.org/10.1111/geb.12681>**

1071 Jarvis, P. G. (1976). The interpretation of the variations in leaf water potential and  
1072 stomatal conductance found in canopies in the field. *Philosophical Transactions of the*

1073 Royal Society of London. B, Biological Sciences, 273(927),  
1074 593-610. <https://doi.org/10.1098/rstb.1976.0035>

1075 Keenan, T., García, R., Friend, A. D., Zaehle, S., Gracia, C., & Sabate, S. (2009).  
1076 Improved understanding of drought controls on seasonal variation in Mediterranean  
1077 forest canopy CO<sub>2</sub> and water fluxes through combined in situ measurements and  
1078 ecosystem modelling. *Biogeosciences*, 6(8), 1423-1444. [https://doi.org/10.5194/bg-6-](https://doi.org/10.5194/bg-6-1423-2009)  
1079 1423-2009

1080 Keenan, T., Sabate, S., & Gracia, C. (2010). Soil water stress and coupled  
1081 photosynthesis–conductance models: Bridging the gap between conflicting reports on  
1082 the relative roles of stomatal, mesophyll conductance and biochemical limitations to  
1083 photosynthesis. *Agricultural and Forest Meteorology*, 150(3), 443-453.  
1084 <https://doi.org/10.1016/j.agrformet.2010.01.008>

1085 Kesselmeier, J., Bode, K., Hofmann, U., Müller, H., Schäfer, L., Wolf, A., ... &  
1086 Torres, L. (1997). Emission of short chained organic acids, aldehydes and  
1087 monoterpenes from *Quercus ilex* L. and *Pinus pinea* L. in relation to physiological  
1088 activities, carbon budget and emission algorithms. *Atmospheric Environment*, 31,  
1089 119-133. [https://doi.org/10.1016/S1352-2310\(97\)00079-4](https://doi.org/10.1016/S1352-2310(97)00079-4)

1090 Kolari, P., Chan, T., Porcar-Castell, A., Bäck, J., Nikinmaa, E., & Juurola, E. (2014).  
1091 Field and controlled environment measurements show strong seasonal acclimation in  
1092 photosynthesis and respiration potential in boreal Scots pine. *Frontiers in plant*  
1093 *science*, 5, 717. <https://doi.org/10.3389/fpls.2014.00717>

1094 Kumar, A., Chen, F., Niyogi, D., Alfieri, J. G., Ek, M., & Mitchell, K. (2011).  
1095 Evaluation of a photosynthesis-based canopy resistance formulation in the Noah land-  
1096 surface model. *Boundary-layer meteorology*, 138(2), 263-284. [https://doi.org/10.1007/](https://doi.org/10.1007/s10546-010-9559-z)  
1097 s10546-010-9559-z

1098 Lin, Y. S., Medlyn, B. E., Duursma, R. A., Prentice, I. C., Wang, H., Baig, S., ... &  
1099 Wingate, L. (2015). Optimal stomatal behaviour around the world. *Nature Climate*  
1100 *Change*, 5(5), 459-464. <https://doi.org/10.1038/nclimate2550>

1101 Loveland, T. R., Reed, B. C., Brown, J. F., Ohlen, D. O., Zhu, Z., Yang, L. W. M. J.,  
1102 & Merchant, J. W. (2000). Development of a global land cover characteristics  
1103 database and IGBP DISCover from 1 km AVHRR data. *International Journal of*  
1104 *Remote Sensing*, 21(6-7), 1303-1330. <https://doi.org/10.1080/014311600210191>

1105 Martin, R. S., Villanueva, I., Zhang, J., & Popp, C. J. (1999). Nonmethane  
1106 hydrocarbon, monocarboxylic acid, and low molecular weight aldehyde and ketone  
1107 emissions from vegetation in central New Mexico. *Environmental science &*  
1108 *technology*, 33(13), 2186-2192. <https://doi.org/10.1021/es980468q>

1109 McKinney, K. A., Lee, B. H., Vasta, A., Pho, T. V., & Munger, J. W. (2011).  
1110 Emissions of isoprenoids and oxygenated biogenic volatile organic compounds from a  
1111 New England mixed forest. *Atmospheric Chemistry and Physics*, 11(10), 4807-  
1112 4831. <https://doi.org/10.5194/acp-11-4807-2011>

1113 Medlyn, B. E., Duursma, R. A., Eamus, D., Ellsworth, D. S., Prentice, I. C., Barton, C.  
1114 V., ... & Wingate, L. (2011). Reconciling the optimal and empirical approaches to  
1115 modelling stomatal conductance. *Global Change Biology*, 17(6), 2134-2144.  
1116 <https://doi.org/10.1111/j.1365-2486.2010.02375.x>

1117 Meyers, T. P., & Baldocchi, D. D. (1988). A comparison of models for deriving dry  
1118 deposition fluxes of O<sub>3</sub> and SO<sub>2</sub> to a forest canopy. *Tellus B*, 40(4), 270-  
1119 284. DOI: 10.3402/tellusb.v40i4.15916

1120 Mills, G., Pleijel, H., Braun, S., Büker, P., Bermejo, V., Calvo, E., ... & Simpson, D.  
1121 (2011). New stomatal flux-based critical levels for ozone effects on

1122 vegetation. Atmospheric Environment, 45(28),  
1123 5064-5068. <https://doi.org/10.1016/j.atmosenv.2011.06.009>

1124 Moss, D. N., Krenzer, E. G., & Brun, W. A. (1969). Carbon dioxide compensation  
1125 points in related plant species. Science, 164(3876), 187-188.  
1126 [10.1126/science.164.3876.187](https://doi.org/10.1126/science.164.3876.187)

1127 Nemani, R. R., Keeling, C. D., Hashimoto, H., Jolly, W. M., Piper, S. C., Tucker, C.  
1128 J., ... & Running, S. W. (2003). Climate-driven increases in global terrestrial net  
1129 primary production from 1982 to 1999. science, 300(5625), 1560-1563. DOI:  
1130 [10.1126/science.1082750s](https://doi.org/10.1126/science.1082750s)

1131 Niinemets, Ü. (2010). Mild versus severe stress and BVOCs: Thresholds, priming and  
1132 consequences. Trends in Plant Science, 15(3), 145– 153.  
1133 <https://doi.org/10.1016/j.tplants.2009.11.008>

1134 Niinemets, Ü., & Reichstein, M. (2003). Controls on the emission of plant volatiles  
1135 through stomata: Differential sensitivity of emission rates to stomatal closure  
1136 explained. Journal of Geophysical Research: Atmospheres, 108(D7).  
1137 DOI:[10.1029/2002JD002626](https://doi.org/10.1029/2002JD002626)

1138 Otu-Larbi, F., Bolas, C. G., Ferracci, V., Staniaszek, Z., Jones, R. L., Malhi, Y., ... &  
1139 Ashworth, K. (2020). Modelling the effect of the 2018 summer heatwave and drought  
1140 on isoprene emissions in a UK woodland. Global change biology, 26(4), 2320-  
1141 2335. <https://doi.org/10.1111/gcb.14963>

1142 Otu-Larbi, F., Conte, A., Fares, S., Wild, O., & Ashworth, K. (2020). Current and  
1143 future impacts of drought and ozone stress on Northern Hemisphere forests. Global  
1144 Change Biology, 26(11), 6218-6234. <https://doi.org/10.1111/gcb.15339>

1145 Padro, J. (1996). Summary of ozone dry deposition velocity measurements and model  
1146 estimates over vineyard, cotton, grass and deciduous forest in summer. *Atmospheric*  
1147 *Environment*, 30(13), 2363-2369. [https://doi.org/10.1016/1352-2310\(95\)00352-5](https://doi.org/10.1016/1352-2310(95)00352-5)

1148 Park, J. H., Fares, S., Weber, R., & Goldstein, A. H. (2014). Biogenic volatile organic  
1149 compound emissions during BEARPEX 2009 measured by eddy covariance and flux–  
1150 gradient similarity methods. *Atmospheric Chemistry and Physics*, 14(1), 231-244.  
1151 <https://doi.org/10.5194/acp-14-231-2014>

1152 Pastorello, G., Trotta, C., Canfora, E., Chu, H., Christianson, D., Cheah, Y. W., ... &  
1153 Li, Y. (2020). The FLUXNET2015 dataset and the ONEFlux processing pipeline for  
1154 eddy covariance data. *Scientific data*, 7(1), 1-27. <https://doi.org/10.1038/s41597-020->  
1155 0534-3

1156 Porporato, A., Laio, F., Ridolfi, L., & Rodriguez-Iturbe, I. (2001). Plants in water-  
1157 controlled ecosystems: active role in hydrologic processes and response to water  
1158 stress: III. Vegetation water stress. *Advances in water resources*, 24(7), 725-744.  
1159 [https://doi.org/10.1016/S0309-1708\(01\)00006-9](https://doi.org/10.1016/S0309-1708(01)00006-9)

1160 Rice, A. H., Pyle, E. H., Saleska, S. R., Hutyra, L., Palace, M., Keller, M., ... &  
1161 Wofsy, S. C. (2004). Carbon balance and vegetation dynamics in an old-growth  
1162 Amazonian forest. *Ecological applications*, 14(sp4), 55-71. <https://doi.org/10.1890/02->  
1163 6006

1164 Rinne, J., Taipale, R., Markkanen, T., Ruuskanen, T. M., Hellén, H., Kajos, M. K., ...  
1165 & Kulmala, M. (2007). Hydrocarbon fluxes above a Scots pine forest canopy:  
1166 measurements and modeling. *Atmospheric Chemistry and Physics*, 7(12), 3361-3372.  
1167 <https://doi.org/10.5194/acp-7-3361-2007>

1168 Rödiger, E., Cuntz, M., Rammig, A., Fischer, R., Taubert, F., & Huth, A. (2018). The  
1169 importance of forest structure for carbon fluxes of the Amazon

1170 rainforest. *Environmental Research Letters*, 13(5), 054013.  
1171 <https://doi.org/10.1088/1748-9326/aabc61>

1172 Royal Society (2008). Ground-level ozone in the 21st century: future trends, impacts  
1173 and policy implications. Science Policy Report 15/08. The Royal Society, London.

1174 Silva, S. J., & Heald, C. L. (2018). Investigating dry deposition of ozone to  
1175 vegetation. *Journal of Geophysical Research: Atmospheres*, 123(1), 559-  
1176 573. <https://doi.org/10.1002/2017JD027278>

1177 SMEAR II (2021). [https://eu-interact.org/field-sites/hyytiala-forestry-research-station-](https://eu-interact.org/field-sites/hyytiala-forestry-research-station-smear-ii/)  
1178 [smear-ii/](https://eu-interact.org/field-sites/hyytiala-forestry-research-station-smear-ii/) last accessed 19/04/2021

1179 Staudt, M., Bertin, N., Hansen, U., Seufert, G., Cicciolij, P., Foster, P., ... & Fugit, J.  
1180 L. (1997). Seasonal and diurnal patterns of monoterpene emissions from *Pinus pinea*  
1181 (L.) under field conditions. *Atmospheric environment*, 31, 145-156.  
1182 [https://doi.org/10.1016/S1352-2310\(97\)00081-2](https://doi.org/10.1016/S1352-2310(97)00081-2)

1183 Steinbrecher, R., Hauff, K., Hakola, H., & Rössler, J. (1999). A revised  
1184 parameterisation for emission modelling of isoprenoids for boreal plants. Biogenic  
1185 VOC emissions and photochemistry in the boreal regions of Europe: Biphorep, Final  
1186 report, Contract No ENV4-CT95-0022, Air Pollution research report, (70), 29-44.

1187 Stockwell, W. R., Kirchner, F., Kuhn, M., & Seefeld, S. (1997). A new mechanism for  
1188 regional atmospheric chemistry modeling. *Journal of Geophysical Research:*  
1189 *Atmospheres*, 102(D22), 25847-25879. <https://doi.org/10.1029/97JD00849>

1190 Suni, T., Rinne, J., Reissell, A., Altimir, N., Keronen, P., Rannik, U., ... & Vesala, T.  
1191 (2003). Long-term measurements of surface fluxes above a Scots pine forest in  
1192 Hyytiala, southern Finland, 1996-2001. *Boreal Environment Research*, 8(4), 287-302.

1193 Wesely, M. L. (1989). Parameterization of surface resistances to gaseous dry  
1194 deposition in regional-scale numerical models. *Atmospheric Environment*, 23 (1989),  
1195 1293-1304

1196 Williams, M., Rastetter, E. B., Fernandes, D. N., Goulden, M. L., Wofsy, S. C.,  
1197 Shaver, G. R., ... & Nadelhoffer, K. J. (1996). Modelling the soil-plant-atmosphere  
1198 continuum in a Quercus-Acer stand at Harvard Forest: the regulation of stomatal  
1199 conductance by light, nitrogen and soil/plant hydraulic properties. *Plant, Cell &*  
1200 *Environment*, 19(8), 911-927. <https://doi.org/10.1111/j.1365-3040.1996.tb00456.x>

1201 Wong, S. C., Cowan, I. R., & Farquhar, G. D. (1979). Stomatal conductance correlates  
1202 with photosynthetic capacity. *Nature*, 282(5737),  
1203 424-426. <https://doi.org/10.1038/282424a0>

1204 Yu, Q., Zhang, Y., Liu, Y., & Shi, P. (2004). Simulation of the stomatal conductance  
1205 of winter wheat in response to light, temperature and CO<sub>2</sub> changes. *Annals of Botany*,  
1206 93(4), 435-441. <https://doi.org/10.1093/aob>

1207